UNIVERSITY OF OKLAHOMA

GRADUATE COLLEGE

EXPERIMENTAL INVESTIGATION OF THE CEMENT BOND INTEGRITY BY APPLICATION OF DIGITAL IMAGE CORRELATION (DIC) TECHNIQUE

A THESIS

SUBMITTED TO THE GRADUATE FACULTY

in partial fulfillment of the requirements for the

Degree of

MASTER OF SCIENCE

By

RAYMOS JEREMY KIMANZI

Norman, Oklahoma

2019

EXPERIMENTAL INVESTIGATION OF THE CEMENT BOND INTEGRITY BY APPLICATION OF DIGITAL IMAGE CORRELATION (DIC) TECHNIQUE

A THESIS APPROVED FOR THE

MEWBOURNE SCHOOL OF PETROLEUM AND GEOLOGICAL ENGINEERING

BY

Dr. Saeed Salehi, Chair

Dr. Catalin Teodoriu

Dr. Deepak Devegowda

Acknowledgements

I would like to thank my Research advisor and mentor Dr. Saeed Salehi for your sacrifices of time, finances and energy during my time as a student. Your devotion to seeing me mature and improve in both my research and academic life has been nothing short of undeserving favor. It has been an honor working with you and learning from you through our discussions and talks about life. I am truly grateful and always in your debt.

I give special thanks to Dr. Catalin Teodoriu for your time and unwavering desire for your students. I am also grateful to Dr. Deepak Devegowda for the opportunity to work with him both during my undergraduate and graduate studies. Thank you both for agreeing to serve on my Thesis committee and for having a listening ear whenever I needed it.

I am grateful to Dr. Khalifeh from Norway for providing the geopolymer samples that were used in this research. This research work was partially supported by the Department of Energy (D.O.E) National Energy Technology Laboratory under Award Number DE- FE0031575 (Tuscaloosa Marine Shale Laboratory). A special thanks goes to the TMSL team at the University of Louisiana for giving me access to both the Material Testing System (MTS) and the Digital Image correlation (DIC) software in order to complete my research objectives.

I would also like to thank Jeff McCaskill from OU WCTC for the coring process, Gary Stowe from the core lab, Jeremy Jernigen and John Sholeen in the Laser Microscopy lab in Sarkeys Energy Center for the assistance in meeting my research objectives timely.

Lastly, I would like to thank my family, parents and two sisters, and my friends for their continual love, prayers and respect for me in my journey in this life.

Table of contents

List of tables

List of figures

Abstract

API Class G and H Portland cements are the most recommended cements for different well operations in order to have good well integrity throughout the life of the well. A loss of zonal isolation is a result of improper cementing jobs which could be a result of inadequate mud displacement, casing eccentricity, mud contamination and mud cake along the formation walls. This has required extensive investigation in order to meet flowability, placement and mechanical properties for particular subsurface conditions. There is limited information on the bonding dynamics of cement after placement. This could provide insight and expound on the detrimental effects of the aforementioned wellbore scenarios. There is also opportunity for research into viable cement systems that could have durable bonds for better well integrity.

This research includes the application of Digital Image correlation (DIC) to critically study the strain development along the cement-steel and cement-formation interface of samples with a formation-cement-steel configuration. Microscope imaging of the interfacial bonds provides a paradigm to explain the formation of the bond as well. These samples were cured for 24 hours at an elevated temperature of 70^{o}C and placed under Indirect Tensile stress conditions. The influence of mud-contamination, casing eccentricity and formation surface roughness on the strain development and the load required to shear the cement bonds was investigated. Two different cement recipes including nano-modified Class H cement and geopolymer cement were compared to Neat Class H cement under the aforementioned conditions as proposed cement systems with sufficient mechanical properties.

1. Introduction

1.1. Research motivation

Natural gas and oil (fossil fuels) were formed by the decay of deposited animal and plant remains (organic) which were converted to these products under imposed high pressures and temperatures over a long period of time. Oil and gas production has increased over the past decade in the United States because of the increased technological emphasis on production from unconventional reservoirs. These advancements mainly include hydraulic fracturing and horizontal drilling which have increased shale oil and gas production with 20 year projections stating up to 17MMbbl/day of oil and 42 Bcf/day from major gas fields as shown in **Figure 1** (EIA 2017). This could change the energy dynamic completely for countries that produce oil and gas on a large scale such as the United States. According to the BP Energy Outlook (2017) edition, the general forecasts for energy consumption by raw material showed that natural gas will account for 9% more than oil by 2035.

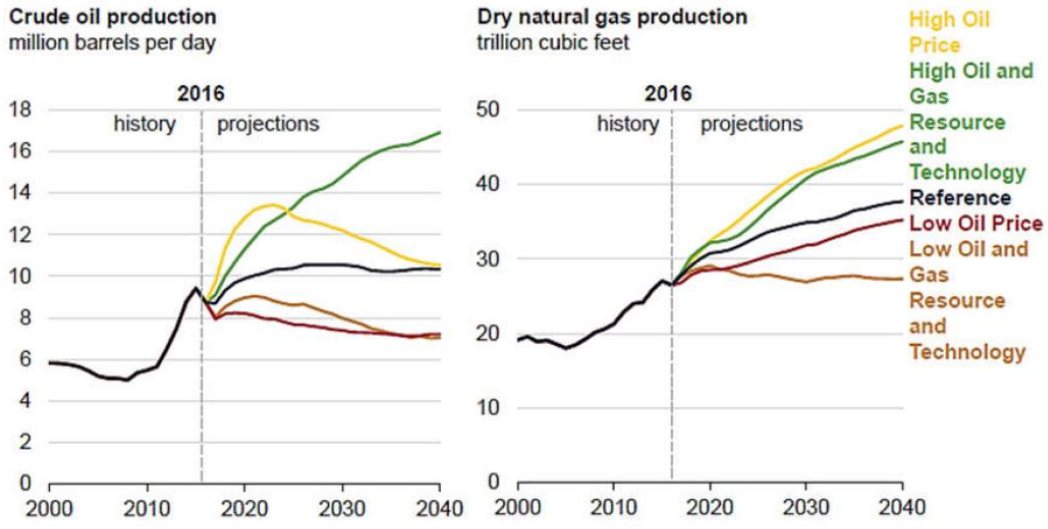

Figure 1- Oil and gas production predictions and factors that influence (EIA 2017)

This predicted increase in production requires that the wells that are drilled should have the durable integrity to enable production of these raw materials to meet worldwide energy demands. There are various well components that enable a safe and conducive pathway for oil or gas from the subsurface under particular conditions. Oilwell cement is one of these well integrity elements which provides a hydraulic seal that establishes zonal isolation, preventing fluid communication and invasion into the wellbore while supporting the casing string. Failing to achieve these objectives may severely limit the well's ability to reach full producing potential.

Therefore, wells are constructed with well barriers in order to mitigate these effects and provide long-term durability in various subsurface conditions such as high temperatures or cyclic operations like CO_2 sequestration and storage (Ichim 2017). A dual-barrier system includes the application of a primary and secondary barrier which are either fluids or mechanical means to prevent fluid flow in the wellbore. Oilwell cement is a primary barrier during the lifetime of the well that is critical for well integrity. There is still a demand for information on the tremendous effects of various subsurface and well properties on the oilwell cement bond with formation or with casing downhole.

There is limited publicly available data on the statistics of the efficiency of cementing operations in various wells constructed in the oil and gas industry. Bonding issues have been cited for a few wells such as Crosby 12-1H well drilled by Goodrich Petroleum Corporation into the Tuscaloosa Marine Shale. This reservoir extends from North-east Louisiana into South-west Mississippi (**Figure 2**).

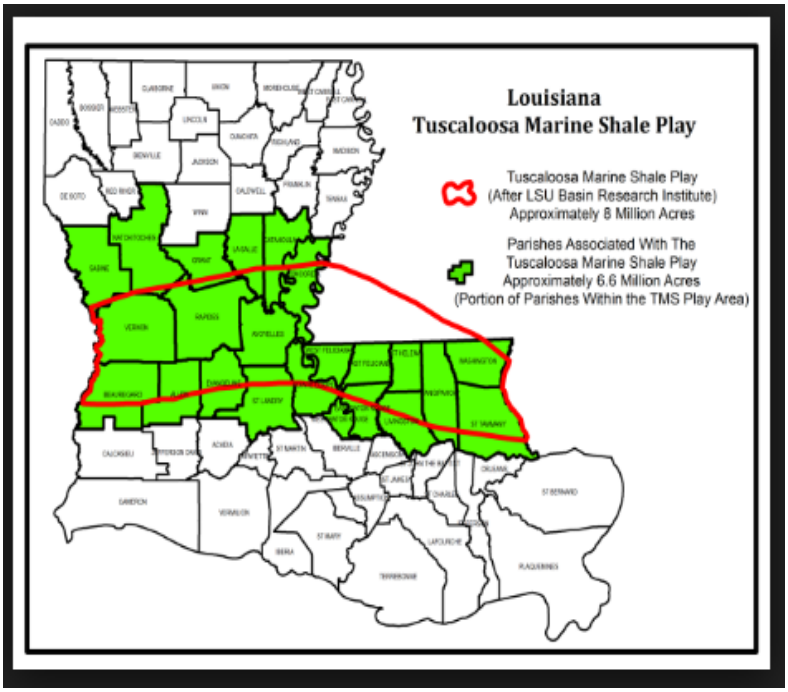

Figure 2 - Tuscaloosa Marine Shale deposit showing location of Crosby 12-1H well (Shale Experts 2016)

The major issues during cementing involved poor bonding in all three sections of the wellbore: surface, intermediate and production. In the surface section, poor bonding was cited as a result of cementing around gumbo shale/weak formation where there was also some lost circulation. In the intermediate section, bonding issues were sited but the direct causes were not mentioned in the drilling reports. There were instances of cement contamination by mud which could have been a major influence on the bonding issues in this section. There were issues of lost circulation and weak formation in cementing the production liner in place at required depth which also led to bonding issues. This required the cementing program to include increase of cement density to increase mud displacement efficiency.

In addition to these aforementioned issues, there are problems caused by casing eccentricity which is linked to poor mud displacement which increases the probability of poor cement bonding.

Casing eccentricity is the degree to which the casing is off-center in another casing or the openhole. During cementing, the cement slurry tends to flow through the larger portion of the hole much faster than through the smaller annulus leading to cement not reaching the layer of the formation to be sealed (**Figure 3**). This is detrimental to the overall well integrity which is discussed in the next section. This research was, therefore, motivated to increase attention to the issues affecting bonding of cement to casing and formation during placement.

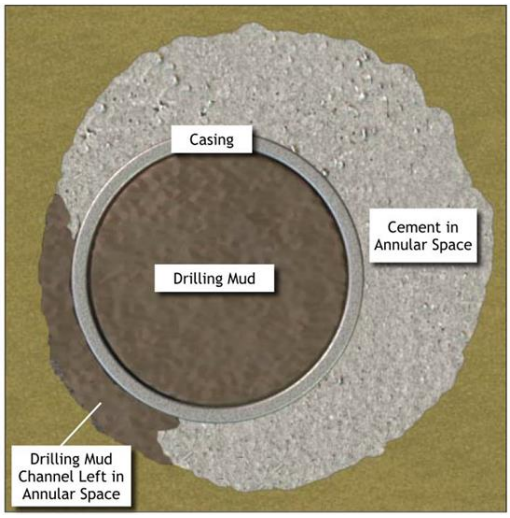

Figure 3 - Casing eccentricity leading to poor mud displacement in smaller portion of annulus (Pegasus Vertex Inc. 2010)

Furthermore, the significance of subsurface structures around the reservoir should be of concern. Loizzo et al. (2017) detailed the effects of geological barriers on the integrity of the wellbore used for injection over time and the required risk analysis in order to carefully predict the potentiality for loss of well integrity. According to this research, creeping rock structures are examples of these barriers: salt and fine-grained siltstones. These barriers could be essential in the prevention or mitigation of gas or liquid leaks from the reservoir in case of failure of the casing-cement-formation system because of their long-term plasticity (Loizzo et al. 2017).

1.2. Research Statement

The NORSOK D-010 document defines well integrity as the application of technical, operational and organizational solutions to reduce the risk of uncontrolled release of formation fluids throughout the life cycle of the well (NORSOK 2004). The document details the different well integrity issues that should be a vital part of any well design and operation in order to prevent or mitigate formation fluid invasion throughout the well's lifetime (NORSOK 2004a). Failure of wellbore integrity is the result of time-dependent formation fluid leakage due to creation of leakage pathways along the well (Kiran et al. 2017; Vrålstad et al. 2018). This could happen at any stage of the well: initial construction, completion, production or abandonment.

With the development of risky environment wells (i.e. high temperature high pressure (HTHP) wells, deep water wells, geothermal wells) and the application of new technologies (i.e. horizontal drilling, water injection, enhanced oil/gas recovery (EOR/EGR), CO2 sequestration), well integrity is becoming one of the most challenging problems because of the complicated loads surrounding and in the wellbore (Ahmed et al. 2019a). As most of potential reasons associate with induced dynamic loading, geomechanical analysis should be considered for preventing the development of leakages of barriers. Possible leakage pathways assuming the cement is elastic or brittle (Thiercelin et al. 1998), are shown in **Figure 4**. The creation of these leakage pathways could be attributed to different factors (Gasda et al. 2004; Nygaard et al. 2014):

1. Casing corrosion and thread leakage due to acidic environments (CO2/H2S with water)

2. Debonding along casing-cement interface

3. Gas migration through created micro-annuli in the cement (Al Ramadan et al. 2019)

4. Incomplete annular cementing

5. Mud channeling during cementing

6. Thermally and mechanically induced fractures in the cement

In addition to negative financial consequences, there are critical environmental effects from subsurface fluid leakages to the atmosphere (Kiran et al. 2017) which could be detrimental and very costly to solve.

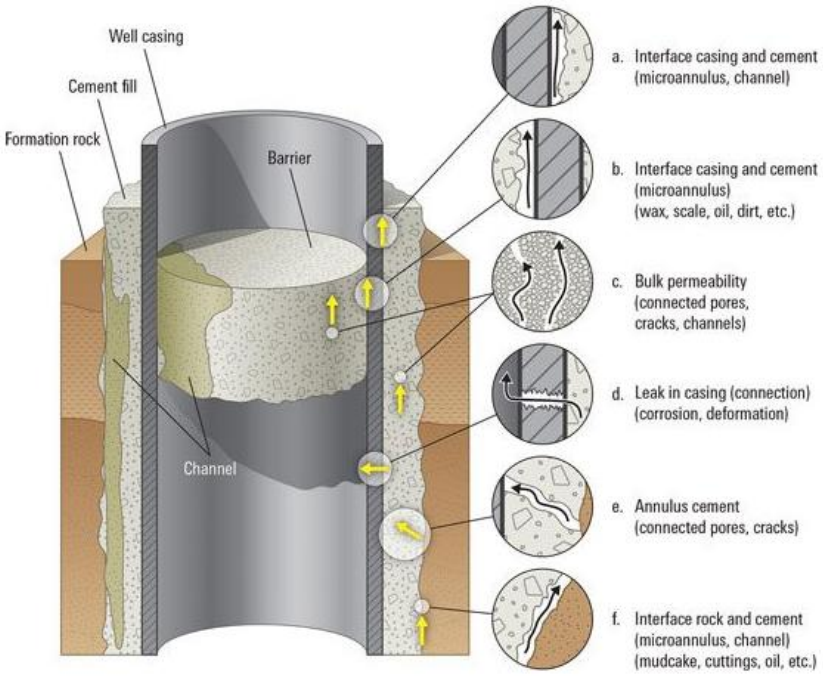

Figure 4 - Potential leakage pathways (Gasda et al. 2004)

Therefore, the cement sheath integrity is a specific part of this study that requires particular investigation with regards to well integrity of the well. The sheath integrity is majorly affected by its mechanical properties and the well operating conditions (Bybee 2002; Garnier et al. 2007; Ahmed et al. 2019b). The critical subsurface conditions include subsurface temperature and pressure conditions, chemical and thermal stresses due to well processes like fluid injection.

In addition to proper zonal isolation of subsurface formations from the wellbore, the cement also prevents fluid invasion from porous formations (Ahmed et al. 2019b). This is the reason why extensive study on the cement and other external sealant characteristics is highly recommended in order to promote the long-term integrity of the well. Bosma et al. (1999) carried out an umbrella investigation on the design approach for sealant selection under extreme subsurface conditions. The researchers carried out mathematical modelling and applied this to set of conditions to determine how tight the seal was. The changes in pressure or temperature that affect the cement sealant, in this case, may be due to production through the wellbore or reservoir depletion, and injection among other factors (Bosma et al. 1999).

Well integrity issues has been a major concern for drilling operations all around the world. This has encouraged research to increasingly alleviate the negative effects of unintentional influx of subsurface fluids into the drilled wellbore. The cementing and casing operations for zonal isolation require that the cement design for these operations is viable for long-term integrity of the wellbore There are significant properties of the cement that are included in the cement design such as compressive strength, slurry pumpability, fast-setting capability that are affected by the cement composition (Patel and Salehi 2019a). The investigation of the bonding dynamics between cement and casing (shear bond) or subsurface formation has been neglected. This is based on the general assumption that a cement sheath created with the proper additives will have a strong and durable bond with both the casing and the subsurface formation (Patel et al. 2019c).

According to Kiran et al. (2017), environmental issues such as contamination of ground water, fluid spills out of the wellbore and escape of subsurface gas to the environment are commonly associated with the deterioration of the cement bond with time. Other factors that influence the integrity of the well throughout its lifetime, in addition to cement quality, are change in

temperature, chemical debonding, corrosion of the casing and increased subsurface pressures (Nygaard et al. 2014; Patel and Salehi 2019b). Uncontrollable factors such as uncentralized casing placements, initial defects of cement near a casing shoe, compositions of cement, and improper mud removal increase the probability of unintentional lower-grade bonding between cement and the casing. These issues have caused recent uproar on the contamination of fresh water aquifers by subsurface fluids through microfractures developed as a result of poor shear and hydraulic cement bonds.

1.3. Objectives

This research effort includes the application of Digital Image Correlation strain mapping and microscope imaging of neat Class H cement, nano-modified Class H and geopolymer bonding to steel and subsurface formations. The main objectives of this work include:

- Investigate the effect of mud contamination on the cement bond with Berea sandstone
- Investigate the difference in bonding of cement with two lithologies: Berea sandstone and Mancos shale.
- Evaluate the effect of eccentricity on the cement bond with steel (“casing”)
- Evaluate the advantage of using nano-modified cement and geopolymer cement over Ordinary Portland cement.

2. Oil well cements

2.1. Cement synthesis

The overall cement composition and placement is significant in order to have a sufficient hydraulic seal that prevents fluid influx into the annular space between the casing and the formation. Based on the synthesis of a particular cement slurry, the resultant mechanical and bonding properties could differ significantly under subsurface conditions during cementing. This section provides information about the synthesis of the different cements that are used for experimentation in this study.

2.1.1. Ordinary Portland Cement

Ordinary Portland cement is the major cement used for synthesis of oil well cement sheaths. Argillaceous (source of silica- SiO_2) and calcareous (source of lime- $CaCO_3$) material are ground and mixed with other material such as gypsum at temperatures around 1500^oC to create an artificial cement blend called Portland cement (**Figure 5**). The overall composition of Portland cement is shown in **Table 1**.

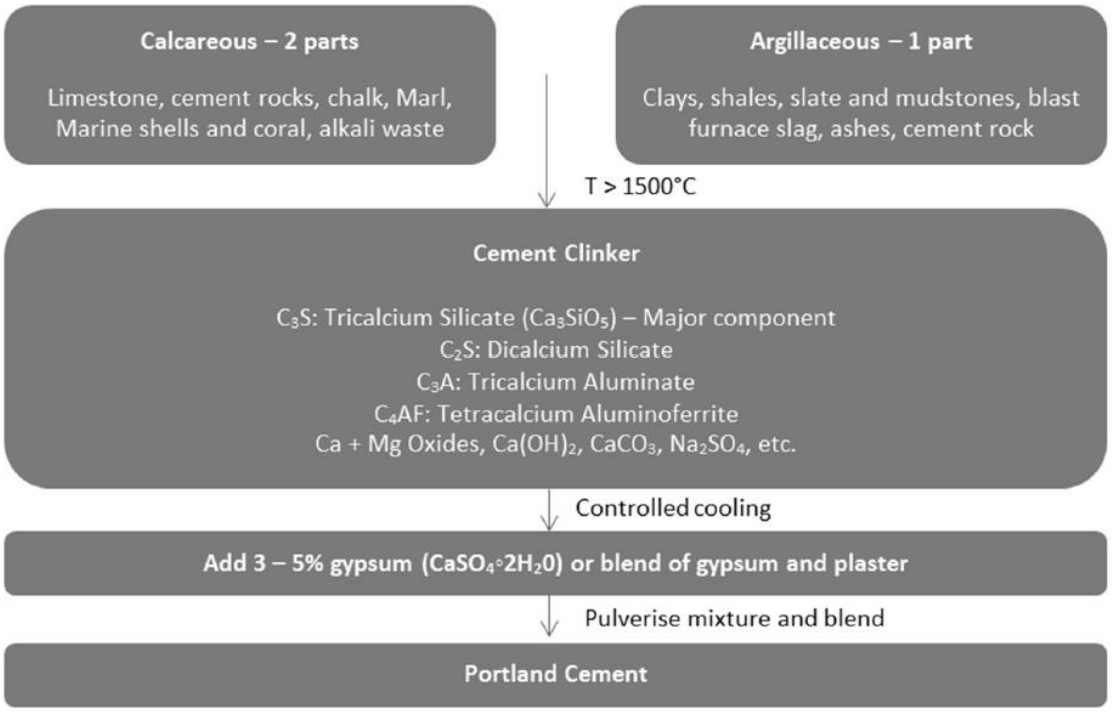

Figure 5 - Portland cement synthesis (Ichim 2015)

Table 1 – Generic composition of Portland cement (Fink 2015)

Compound	Percentage
Calcium oxide CaO	60-69
Silicon dioxide SiO_2	18-24
Aluminium oxide Al_2O_3 and Titanium oxide TiO_2	4 8
Iron oxide Fe_2O_3	1 8
Magnesium oxide MgO	<5
Sulfur trioxide SO_3	<3
Potassium oxide K_2O	<1
Natrium oxide Na_2O	<1

There are eight different cement classes of oil well cements according to American Petroleum Institute (2010):

- Class A – For depths less than 6000 ft when special properties are not required.

- Class B – For depths less than 6000 ft with requirements for moderate to high sulfate resistance.
- Class C – For depths less than 6000 ft with requirements for high early strength and high sulfate resistance.
- Class D – For depths between 6000 ft and 10000 ft with requirements for moderate and high sulfate resistance and to counter moderately high temperatures and pressures.
- Class E – For depths between 10000 ft and 14000 ft under high temperature and high pressure conditions for moderate and high sulfate resistance.
- Class F – For depths between 10000 ft and 16000 ft under extremely high temperature and high pressure conditions for moderate and high sulfate resistance.
- Class G and H – For depths less than 8000 ft. Accelerators and retarders to cover a range of depths and temperatures for moderate and high sulfate resistance. Class G cement has finer particle size and therefore requires more water for mixing than Class H which is coarser.

Table 2 shows the major crystalline compounds in the powder cement that hydrate in order to form the rigid cement structure after mixture with water (Bourgoyne et al 1991). The hydration reaction of C_3S with water is a fast reaction that results in the formation of Calcium-silicate hydrate gel which contributes to early cement strength during the first month (28 days) of curing. C_3A hydration reaction is also rapid and produces the required heat energy for the hydration reaction. C_2S reacts with water and is a slow reaction that majorly influences the long term strength of the rigid cement structure. C_4AF is considered minor in its effects on the physical properties of the cement sheath both short and long term. The hydration of powdered cement therefore leads to liberation of heat, change in volume and leads to mechanical bonding (Aïtcin and Flatt 2016). The

other products of hydration include crystalline Calcium hydroxide ($Ca(OH)_2$), monosulfoaluminoferrite and trisulfoaluminoferrite hydrates.

Table 2 – Four major compounds that hydrate to form cement rigid structure ((Bourgoyne et al 1991).

Compound	Formula	Designation
Tricalcium silicate	$3CaO.SiO_2$	C_3S
Tricalcium aluminate	$3CaO.Al_2O_3$	C_3A
Dicalcium silicate	$2CaO.SiO_2$	C_2S
Tetracalcium aluminoferrite	$4CaO.Al_2O_3.Fe_2O_3$	C_4AF

During curing of the cement as it hydrates, the cement slurry experiences a reduction in volume called shrinkage which has been estimated to be between 1% and 8% reduction depending on slurry design (Aïtcin and Flatt 2016). Research has been conducted on the degrading effect of cement shrinkage on the radial and circumferential stresses of the created cement sheath (Dusseault et al. 2000). This is usually due to creation of fractures along the casing-cement interface In addition to creation of micro-annuli in the cement, the propagation of such fractures during the use of the well increase the permeability of the cement and loss of well integrity over the life of the well.

Various additives are used in the field to precisely change the physical and chemical properties of the cement such as density (barite, bentonite, diatomaceous earth), thickening/setting time (sodium chloride, calcium chloride) and filtration. Silica flour is vital in field operations for cementing especially in high temperature applications to reduce the detrimental effects (shorter thickening time and lower strength) of the large transfer of heat. Portland cement has been the primary material for zonal isolation in oil and gas wells but over the last 20 years, it has been discovered that the long-term properties of the cement sheath change drastically. These include the durability

in corrosive environment, susceptibility to mud contamination, low ductility, long-term chemical instability and thermal instability (Vrålstad et al. 2016; Jafariesfad et al. 2017; Saleh et al. 2018). These negatively affect the overall well integrity and life cycle of the wellbore.

2.1.2. Geopolymerized cement

As an alternative binder to Portland cement, geopolymerized cement has been of interest in both construction/civil engineering and petroleum industries over the last 20 years. Geopolymers have been proven to have higher mechanical strength, durability and lower shrinkage compared to Ordinary Portland Cement (Salehi et al. 2016a; Khalifeh et al. 2017a). Geopolymers are inorganic polymers similar to natural zeolitic materials with an amorphous microstructure (Davidovits 1999). Geopolymerized cements are synthesized by the alkali activation of alumino-silicate materials to form an aluminosilicate gel at a temperature greater than 120^{o}F (Salehi et al. 2016b; Khalifeh et al. 2018). This reaction occurs under three mechanisms: dissolution, transportation/reorganization and polycondensation (Davidovits 2011) shown in **Figure 6**.

Alkali dissolution of the solid aluminosilicate based materials results in a supersaturated aluminosilicate solution and the dissolution of alumina silicates results in the formation of oligomers (Duxson et al. 2007). Water is not chemically present in the geopolymerization reaction. Polymerization and hardening are functions of curing time (Rangan 2014) and are the last processes. The type of source material influences the quality of these resultant geopolymerized cement. The result of the polymerization process is a three-dimensional polymeric chain and a ring structure that comprises Si-O-Al-O bonds (Davidovits 1999) shown in **Equation 1**.

$$\underset{\text{(Si-Al materials)}}{n(Si_2O_5.Al_2O_2) + 2nSiO_2 + 4nH_2O + NaOH \text{ or } KOH} \rightarrow Na^+,K^+ + n(OH)_3\text{-Si-O-}\underset{\underset{(OH)_2}{|}}{\underset{\text{(Geopolymer)}}{Al^-}}\text{-O-Si-}(OH)_3 \quad (1)$$

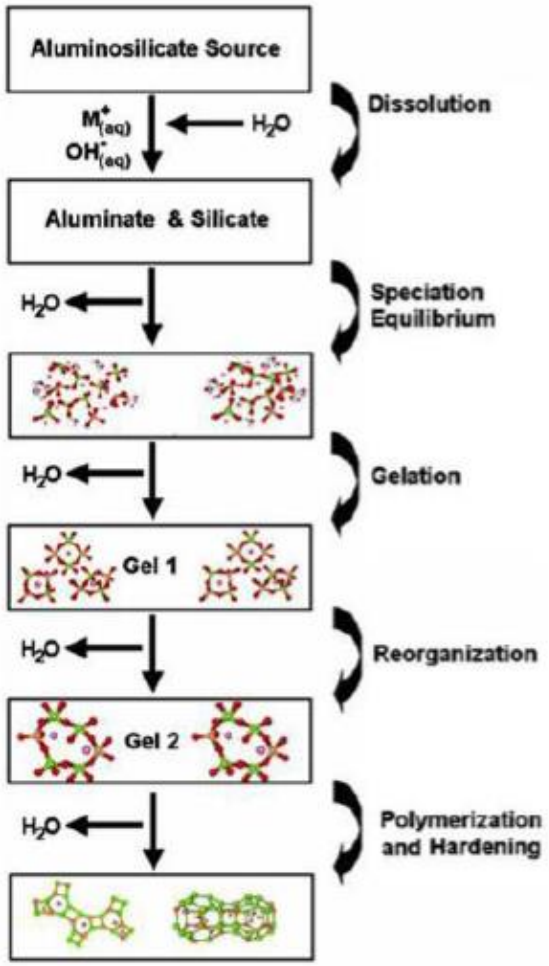

Figure 6 – Synthesis of geopolymerized cements (Duxson et al. 2007)

During curing, water is removed from the geopolymer structure leading to the creation of nanopores which is beneficial to the performance of the binding material (Khalifeh et al. 2017b) unlike Portland cement. During hydration of Portland cement, the existence of any free water reduces cement strength and increases porosity and permeability (Bourgoyne et al. 1991). The source material components for the polymerization reaction must have high contents of Silicon and Aluminum. Clay-rich, kaolinite-rich and blast furnace by-product materials such as slag, fly ash are viable options as source materials (Khalifeh et al. 2015). The expense, availability, and

type of application majorly influence which source material is used especially in the construction industry.

The two concentrated alkaline fluids that are usually sodium hydroxide (NaOH) or potassium hydroxide (KOH) (Rangan 2010). Increasing the molar concentration of the alkaline activators could be detrimental to the bond strength and decreasing the concentration highly affects the binder strength (Bwala 2015). Other factors such as curing temperature and contact time with alkali activators affect the formation of the geopolymeric bond and its bond strength with any material.

Research has gone into discovering the viability of these inorganic binders as potential substitutes to the Portland cement. Experiments on the long-term durability of rock-based geopolymers showed the compressive and tensile strength of geopolymers increase when in contact with crude oil or brine (Khalifeh et al. 2016). This research also concluded that geopolymers have very low permeability even when exposed to hydrogen sulfide (H2S) which causes chemical deterioration in Portland cements (Kiran et al. 2017).

In addition, research on the effect of oil-based mud contamination showed that the geopolymer compressive strength was much less affected than in Neat Class H cement as shown in **Figure 7** (Salehi et al. 2016b). It has also been discovered that geopolymers have high stability (no cracking) at high temperatures and very low chemical shrinkage (Salehi et al. 2016b; Paiva et al. 2018). Some properties of the geopolymers such as pumpability (thickening time), highly affected by temperature, and contamination by water-based muds still require more investigation.

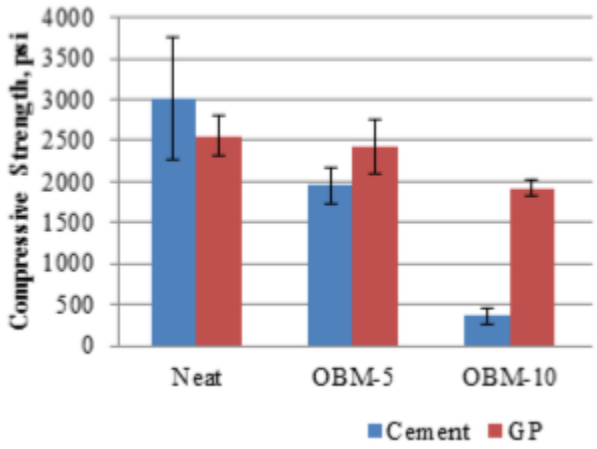

Figure 7 - Comparison of compressive strength tests of mud contaminated (5% and 10% by mass) Portland cement and Geopolymer (Salehi et al. 2016b).

2.2. Bonding theory

The bond between cement and the steel/casing or formation is formed by adhesion between the two materials in contact. This adhesive bond strength is a function of the resistance to separation between the two bonded surfaces. Displacement across the interfacial bond provides a reference to the strength of the bond (Wilson et al. 2018). This behavior is usually assumed and tested/logged for macro scale bonding which is not truly representative of the generation of stresses across the interface. The limitations of some of main wellbore logs regarding cement bonding are shown in **Table 3**. The adhesive bond between the cement and casing/formation is a collection of smaller bonds across the interface rather than one single large bond (Wilson et al. 2018) as shown in **Figure 8**.

Table 3 - Limitations of various wellbore logs (Kiran et al. 2017).

Logs/Surveys	Uses	Limitations
Cement Bond and Variable Density Logs	Predicts well-bonded cement, debonding at wet casing and formation	No prediction of mud channels, vertical cracks, gas chimney, and radial variation in cement
Ultra-sonic imaging log	Shows well-bonded cement, mud channel in good cement, gas chimney, and debonding at wet casing	Unable to figure out mud channels in weak cement, vertical cracks, debonding at dry casing and formation, and radial variation in cement
Isolation Scanner	Capable of showing good cement, mud channels, gas chimneys, thick vertical cracks, debonding at wet casing and formation, and cement radial variation	No prediction on thin vertical cracks and debonding at dry casing

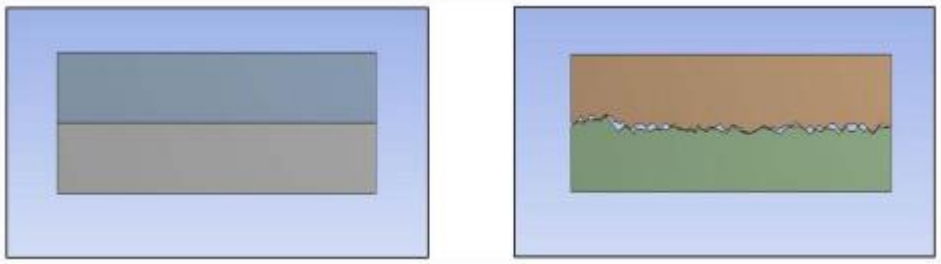

Figure 8 - Bond model with continuous contact (left). A bond with discontinuous contact but collection of small bonds (right) (Wilson et al. 2018).

It is evident that these two bond types would fail differently. The continuous contact interface will fail completely under particular shear stress conditions while the individual small bonds in the discontinuous contact model fail at different intervals. Under similar stress conditions, the discontinuous bond will still be intact though weaker, as shown in **Figure 9**.

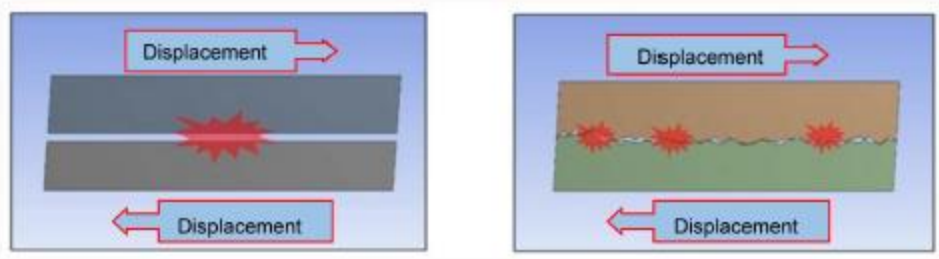

Figure 9 - Failure under shear stress conditions. Continuous bond model complete failure (left). Irregular failure in discontinuous bond yet still intact (right). (Wilson et al. 2018)

The bond between the cement adhesive and the casing or formation follows the mechanical bonding theory. This bond is formed when the cement gel structure flows into the surface cavities or pores on the casing or formation surface and hardens creating a mechanical interlocking bond This process is greatly enhanced by the ability of the adhesive to critically penetrate the pores (rheological properties) and wet the surfaces displacing the air forming the mechanical bond (Bwala 2015). In addition, the roughness of the substrate surface (casing or formation) increases the surface contact area onto which the cement adhesive can interlock with. Therefore, the higher the number of cavities (peaks and valleys) on the substrate surface, the higher the probability of a stronger mechanical bond with cement.

The adhesive bond is stronger with roughness because the shear force required to overcome the high friction and completely disintegrate this bond is increased compared to smooth surface bond. It is imperative to note that the effect of roughness is only possible if the adhesive can wet the surface initially (Bwala 2015). Therefore the quality of the adhesive is a major influence on the formation of the frictional adhesive bond. It has been recommended that the mechanical characteristics of a cement system that can withstand the operational load cycling over time (ductile) are as follows (Williams et al. 2011):

- The higher the ratio of tensile strength to the Young's modulus, the more favorable the cement is to elevated temperature, pressure and cyclic stresses.
- The suitable ratio of cement Young's modulus to formation Young's modulus is 0.5.

2.2.1. Effect of casing roughness on shear bond

Evans and Carter (1962) defined the shear bond strength as the force required to overcome the mechanical bond between the cement and the casing, while the hydraulic bond is that between the cement and the formation. From their research, they carried out experimental investigations on the effect of temperature, roughness and mud contaminations on the shear bond strength of Portland cement with pipe. Their results showed that increase in temperature led to thermal expansion of the casing which created stress on both the shear bond and in the casing itself. Regarding the bond strength, used rusty pipe had a much higher bonding strength compared to a smoother mill finished pipe as shown in **Table 4**.

Table 4- Effect of surface roughness on shear bond adapted from Carter and Evans (1964)

Steel	Bond Strength	
	Shear	Hydraulic
Type of finish	(psi)	(psig)
New (Mill Varnish)	74	200-250
New (Varnish chemically removed)	104	300-400
New (Sandblasted)	123	500-700
Used (rusty)	141	500-700
New (sandblasted-resin-sand coated)	2400	1100-1200

Scott and Brace (1966) observed the bond strength of casing-cement is improved by a rough casing surface. Resin-sand coating is used to accelerate the roughness and it keeps an excellent bond strength in high temperature conditions (i.e. 300-400°F).

2.2.2. Effect of mud contamination

The harmful effects of treated mud sheaths contaminating the cement slurries during placement were also investigated by Morgan and Dumbauld (1952). The research revealed that there was significant reduction in the tensile strength of the hardened cement. This was a result of the chemicals within the treated muds that altered the cement structural and rheological properties leading to low cement strength (**Figure 10**) and poor bonding to the casing.

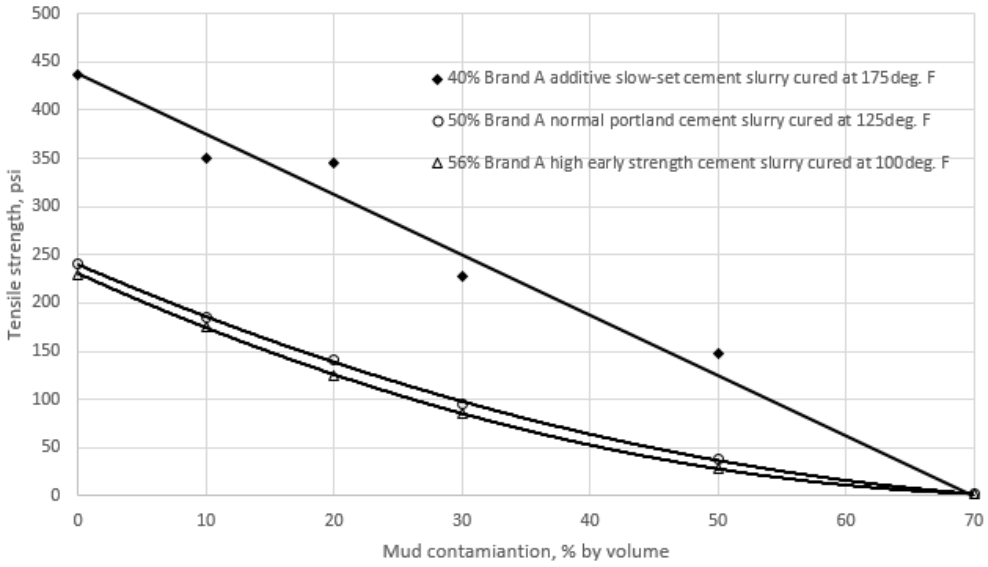

Figure 10 - Effect of mud contamination on tensile strengths of three types of oil well cements (from Morgan and Dumbauld 1952).

There has been an increased application of oil-based muds in unconventional reservoirs such as deeper High Pressure/High Temperature zones over the last two decades. Research has shown that oil-based muds are more stable at higher reservoir temperatures (higher failure temperatures than water-based fluids (Amani et al. 2012). Research into the contamination of cement by oil-based muds has proven detrimental to the integrity of the cement sheath. The results have shown an increase in porosity, detrimental decrease in cement compressive and shear bond strength in addition to changes in the thickening time of the slurry (Carter and Evans 1964; Li et al. 2016). There is also noted reduced probability of wetting of the substrate surfaces by the cement slurry

leading to reduction in bond strength with casing and formation (Peterson 1963). **Table 5** shows results on the shear bond tests done on different drilling fluid systems to show the larger negative effect of oil-based mud.

Table 5 - Effect of mud type on shear bond strength adapted from Carter and Evans (1964)

Type of Mud	Shear Bond (psi)
None	141
Water base	97
Inverted Oil Emulsion	66
Oil base	63

It is also critical to note that existence of a layer of mud cake along either the formation walls or the outer portion of the casing during cement placement leads to failure of creation of a cement bond seal (Nath et al. 2018). This critically affects the short and long term well integrity. This has led to intense investigations into increasing the drilling fluid displacement and cleaning of the casing and formation surfaces before cement is pumped down into the annulus (Ma et al. 2007).

2.2.3. Effect of casing centralization on cement bond

For successful primary cementing operation, to prevent mud channeling, cement placement in the annulus requires a frictional pressure drop should overcome the gel strength of the mud (Xie et al. 2015). Casing will tend to be eccentric to the wellbore in deviated and horizontal wellbores and usually results in gelling of the mud along the narrow annulus because the mud flows much slower (Ryan et al. 1992). This makes it harder for the preflush or spacer to clean the wellbore and prepare it for cementing. There are instances when the casing eccentricity is a result of hole enlargement or caving in of the formation. If the casing is run with a limited number of centralizers, the probability of casing eccentricity increases exponentially which leads to well integrity issues during the lifetime of the well (Matsuzawa et al. 2006). There is also increased possibility of casing

collapse as a result of non-uniform loading during different operations of the well (Guohua et al. 2012). **Figure 11** shows the difference between a concentric and eccentric casing.

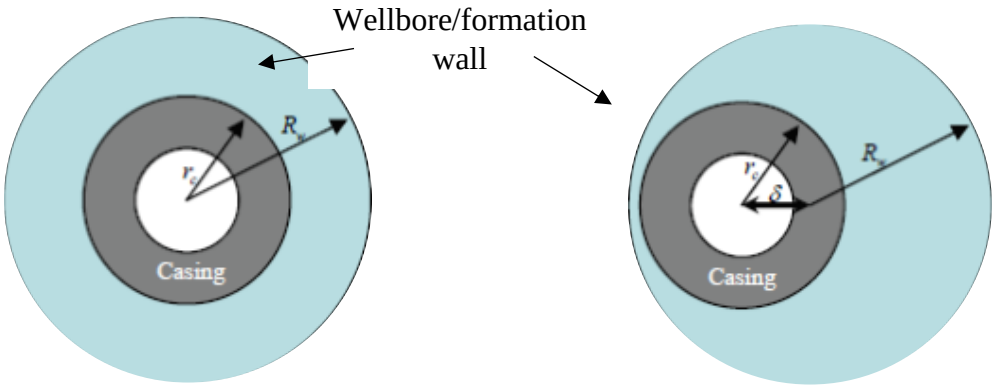

Figure 11 – Schematics of casing placements in a wellbore: concentric (left) and eccentric (right) (Salehabadi et al. 2010)

The degree of eccentricity is calculated using **Equation 2** below and is a value between zero (concentric) and 100% (touches the wellbore/formation wall) (Salehabadi et al. 2010)

$$\text{Eccentricity\%} = \frac{\delta}{(R_w - r_c)} * 100 \quad \text{.....(2)}$$

Casing eccentricity is rarely accounted for in cementing calculations as the wellbore is assumed to have a concentric casing which is very inaccurate especially in deviated holes (Ferda and Al-Ghadban 2004). Since the 1940s, it has been recommended practice to keep the drilling mud and cement separate using spacers/preflushes. Couturier et al. (1990) investigated the effect of mud removal in the conditions of eccentric annuli in order to define spacer design conditions. They discovered that the rheology (density, viscosity and gel strength) of the spacer relative to the drilling mud and the cement is the most critical in its design.

Andrade et al. (2014) tested the relationship between casing centralization and cement bonding (**Table 6**). The results determine that a centralized casing has negative effects on the bonding of

both casing-cement and cement-formation interfaces without consideration of thermal effects. After applying thermal cycling, the deterioration of casing-cement bonding is more severe in the scenario with 50% casing stand-off. It can be explained by the uniformed thermal loading on the cement to make the location with large tensile radial stress to excess the bond strength easier than centralized casing.

Table 6 -The percentage of casing-cement and cement-formation bonding in the centralized casing scenario and 50% stand-off scenario respectively.

Sample	Bonding	Before cycling	After cycling
Centralized	Casing-cement (%)	79	77
	Cement-formation (%)	97	96
50% stand-off	Casing-cement (%)	93	82
	Cement-formation (%)	99	99

2.2.4. Shear bonding experimental methods

There has been investment into studying and providing solutions for Portland cement bonding issues over the last 50 years. Teodoriu et al. 2018 investigated shear failure and bonding stresses of Neat Class H cement using the two set ups as in **Figure 12**. Under the effect of curing time, it was concluded that the shear strength of Neat H cement is higher than the shear bonding strength. The pure shear strength was calculated using **Equation 3** and the shear bonding strength was calculated using **Equation 4**. This would imply that debonding along the cement-casing interface occurs before the cement sheath fails under shear stress.

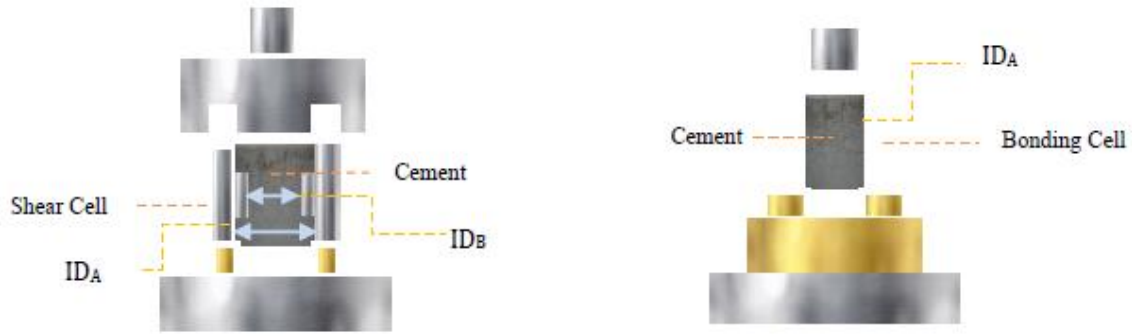

Figure 12 – Pure shear strength (left) and shear bonding strength (right) set ups (Teodoriu et al. 2018)

$$\sigma = \frac{F_{max}}{2\pi * ID_B * SL} \quad \text{.....(3)}$$

$$\sigma = \frac{F_{max}}{2\pi * ID_A * CL} \quad \text{.....(4)}$$

In addition, Jadhav et al. (2017) carried out experiments to measure the effect of casing coating on the shear bond strength of Class G cement with a defoamer and free water control agent added. The experimental set up is similar to Teodoriu et al. (2018) as shown in **Figure 13**. They discovered that the shear bond strength with inorganic coating was twice that of the pipe without coating. The recommendation from this research is that the casing pipes in the field should be coated.

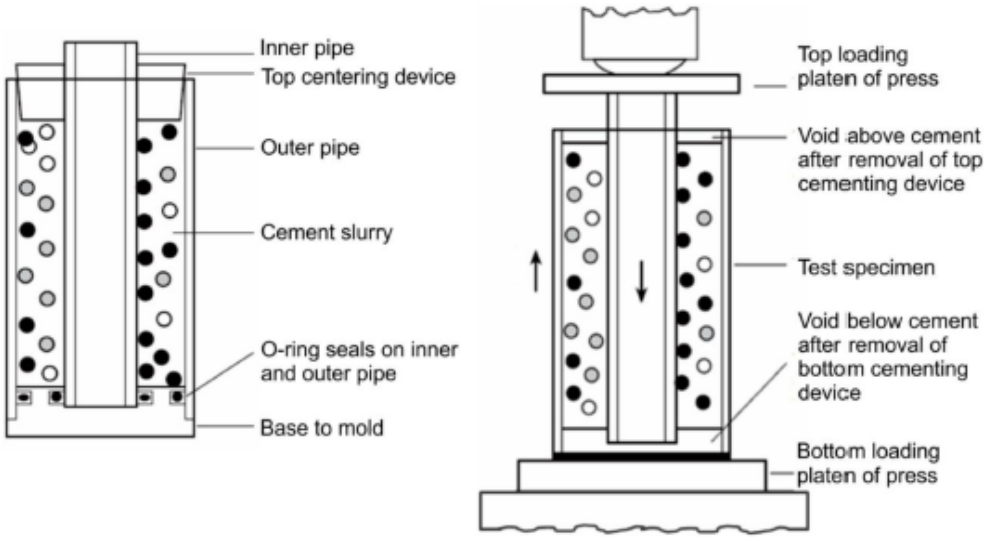

Figure 13 – Schematic of setup using hydraulic press to measure shear bond strength (Jadhav et al. 2018)

Regarding shear bond strength of geopolymers, Salehi et al. (2017) carried out characterization and shear bond strength tests of geopolymer (different molar concentrations of alkali activator) using two different pipes: one with mill coating and the other without. The shear bonding setup is shown in **Figure 14**.

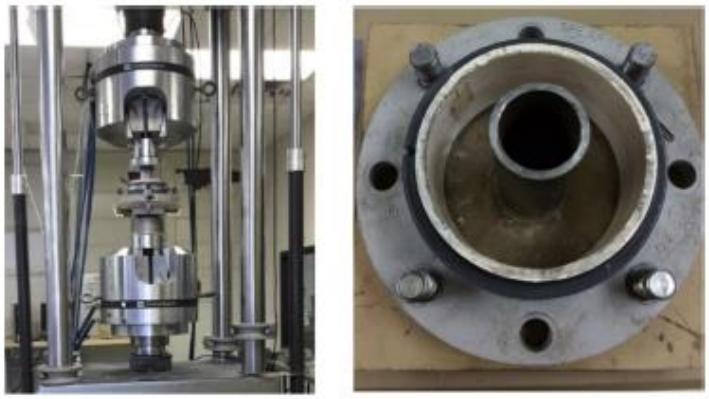

Figure 14 – Experiment setup for shear bond strength test of geopolymer cement (Salehi et al. 2017)

Neto et al. (2014) investigated the bond strength between Portland cement and steel. The substrate surfaces were initially wetted in three different ways: a) washed with water and dried with ethanol, b) chemically treated with NaCl on the surface and c) coated with a layer of cement dried before placing it in a mold. Their research showed that steel chemically treated with NaCl showed strongest shear bonding comparatively. It was suggested that chlorine ions influenced the process of corrosion of the steel creating a rougher substrate surface leading to the formulation of a stronger adhesive bond.

2.3. Addition of nano-synthetic graphite

In addition to geopolymer cements, the addition of nano particles in Portland cements especially Class G and H has been a major area of study over the last decade. Due to the cement shrinkage during the hydration of cement and low tensile strength, research has gone into development of cement additives such as nano-synthetic graphite. Graphites have been tested at different levels in different industries to have various advantages. These advantages include good thermal and electrical conductivity, corrosion shielding and others (Asbury Carbons 2018). Graphite's properties make it multifaceted in its purpose: lubrication, thermal and electrical conductivity, corrosion shield among others which makes it advantageous to the oil and gas cementing industry (Peyvandi et al. 2017). The nanosynthetic graphite used in this research comprised of the different components shown in **Table 7**.

Table 7 – Components of Nanosynthetic graphite (Asbury Carbons 2018)

Property	Value	Units
Carbon	99.94	%
Sulfur	0.009	%
pH	6.05	
Surface area	325-375	m^2/gram
Density	2.16	g/cc

Due to the large surface area of these nano particles, the integration of these materials in cementing designs has resulted in a more uniform cement slurry with higher and more stable mechanical properties. These include reduced permeability, increased compressive and tensile strength which are vital for the annular seal (Patil and Desphande 2012; Ahmed et al. 2018; Kimanzi et al. 2019).

Figure 15 shows the compressive strength of nano-modified class H showing the faster generation of compressive strength (21.8% higher) than Neat Class H under ambient curing conditions (Ahmed et al. 2018).

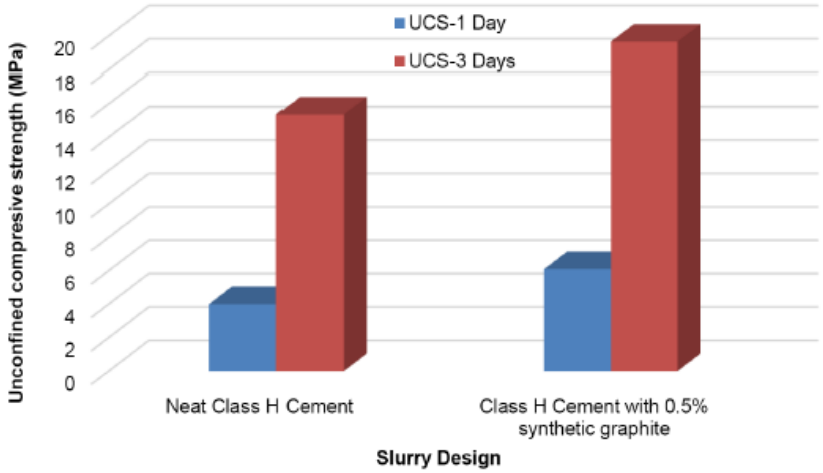

Figure 15 – Comparison of Unconfined compressive strength due to nano-modification (Ahmed et al. 2018)

There is limited information about the bonding dynamics involved with nano-modified cement which is part of this research work to compare that to Neat Class H.

3. Experimental design and methodology

This section focuses on the materials, design of experiments and the assumptions behind the different parts of the experimental methodology. Explanations are also provided as justifications of the different equipment that were applied.

3.1. Materials

Table 8 shows the cement system designs and composition that were studied for this research. The total volume for the cement slurries was kept constant at a mean value of 600 ml for consistency.

Table 8 - Cement slurries and composition

	Component	Amount	Units
Geopolymer	Precursor	700	g
	Potassium hydroxide solution	350	ml
Neat Class H	Cement	859	g
	Water (38% BWOC)	326.4	g
Nano-modified Class H	Cement	859	g
	Water (38% BWOC)	326.4	g
	Nano graphite (0.5% BWOC)	4.3	g

*BWOC – By Weight of Cement

Berea sandstone and Mancos shale were the two formation cores that were used for the sample design. Mancos Shale formation was deposited along the steep margin of the Western Interior Seaway during the cretaceous time period (Kauffman et al. 1984) with many layers of calcite, clays and quartz. Berea sandstone formation was deposited in the Appalachian basin in the Late Devonian period and has been a benchmark for conventional reservoir research. These two formations were the main focus for this research to investigate whether cement bond integrity is similar in conventional and unconventional (majorly shale) reservoirs. The mineral compositions

of the Berea sandstone and Mancos shale are shown in **Table 9** and **Table 10**. Berea sandstone has an average Young's modulus of 25 GPa and Poisson's ratio of 0.33 while Mancos shale has 7 GPa Young's modulus and Poisson's ratio of 0.25. This means that Berea sandstone is more brittle compared to Mancos shale. The cylindrical specimens used in this research were cored using a diamond-coated bit at the same RPM for consistency, cut and polished by the same person, me.

Table 9 - Mineral composition of Berea sandstone (Dawson et al. 2014)

Mineral	Proportion %
Quartz	90.6
Potassium feldspar	4.1
Anorthite	3.2
Kaolinite	1.5
Ankerite	0.4
Dolomite	0.2

Table 10 - Mineral composition of Mancos Shale (Zhang and Sheng 2018)

Mineral	Proportion %
Quartz	55
Total clay	15*
Ankerite	12
Calcite	8
Plagioclase	5
Potassium feldspar	3
Siderite	1
Pyrite	1

*Most documented research state Mancos clay contains an average of 20% clay.

Clay mineral	Proportion %	
Mixed-layer clays	61	mixture of illite (30%) and montmorillonite (70%)
Illite	30	
Kaolinite	7	
Chlorite	2	

3.2. Sample design

The sample setup was meant to be a portrayal of a generic wellbore shown in **Figure 16.**

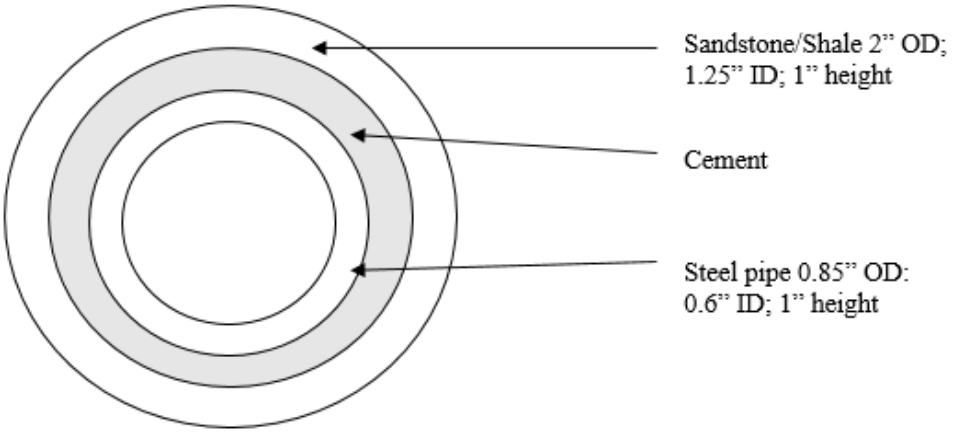

Figure 16 - A generic experimental setup for the samples

Cement samples were prepared in a commercial blender with 3.5 hp with keypad to adjust speed setting (rpm) (**Figure 18a)** according to API recommendations: at 4000 RPM for 15 seconds, during which all solid components were added to the liquid components in the mixer, and then 12000 RPM for 35 seconds. The blender was reconfigured to provide the mixing energy that is provided by API 10B-2 guidelines. It is common that the field and laboratory tested properties of cement slurry have little to no correlation which may be an issue for well integrity (Saleh et al. 2019). For reference, the mixing energy under the above API cement mixing recommendations is 5.9 kJ/kg. The mixing energy was kept consistent for all the cements throughout the study because the thickening time of the cement slurries has been investigated to decrease with increase in mixing energy (Hibbert et al. 1995).

The mud samples used in this experiment were prepared as in **Table 11** to attain a water-based mud with density of 10 lbm/gal that is equivalent to a field sample. The two main drilling fluids

used during oil well drilling are water-based and oil-based muds. This research focuses on water-based mud contamination to provide a baseline for cement-contamination which usually occurs when drilling the intermediate sections of the well. Preliminary testing was carried out using the same sample configuration with varying mud contaminations: 1%, 5%, 10% and 20% by volume. In addition to results attained from Nath et al. (2018) on detrimental effects of mud contamination (10% and 20%) on the cement bond with steel (**Figure 22**), 10% mud contamination by volume was chosen for this experimental design. For consistency of final mixing volume of 600 ml, neat class H was mixed with water to a volume of 540 ml and 60 ml was added to the cement slurry with application of 4000 rpm for 10 seconds to simulate field contamination.

Table 11 - Drilling mud components

Component	Mass (g)
Water	319.16
Bentonite	20
Caustic soda	0.5
Lignite	4
Desco	4
Barite	72.82

A degree of eccentricity of 50% was used for this study because it was the minimum degree that could still allow for cement to enter the smaller end of the annulus. This would also provide the baseline for experimentation of the bond integrity. In horizontal wells, even with the addition of centralizers, there is still high probability of higher degrees of eccentricity (70 – 100%) in long laterals. API recommends a casing eccentricity lower than 64% in order to still have wellbore integrity. This is predominantly in wells constructed for unconventional reservoir production. During the deformation sequence, the samples with eccentricity were positioned to represent a

horizontal wellbore with the casing tending to sit at the lower end against the formation. This meant that the steel pipe was in the sample configuration as shown in **Figure 17**.

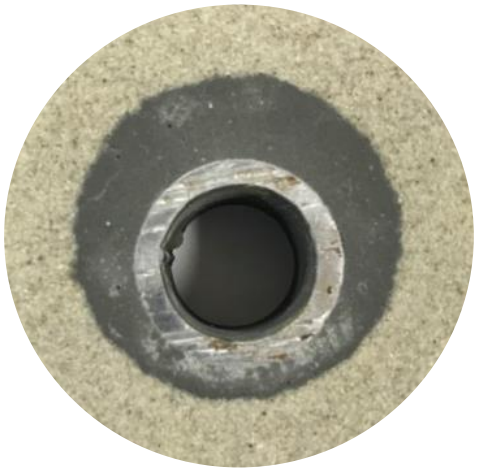

Figure 17 – Sample configuration showing 50% pipe eccentricity

Sample configurations are shown in **Table 12**. The number of samples includes both those used in preliminary tests in May 2018 (Neat Class H, mud-contaminated H and eccentric cases) and those tested early April 2019 (all cement systems). Since the DIC experimentation was carried out in University of Louisiana at Lafayette, there were time and financial constraints which affected the choice for number of samples tested. This was in addition to the costs to procure the core samples. The samples were placed in a 2010 Thermo Scientific Precision 2835 180 series water bath that was set at a static mean temperature of 158^{o}F ± 9^{o}F (70^{o}C ± 5^{o}C) as shown in **Figure 18b**. All the samples were cured at this temperature for 24 hours before transferring them for microscope imaging and DIC testing under Brazilian strength test conditions. No pressure was imposed during curing but for further studies, this could be part of the experimental design. Ambient curing conditions were applied as recommended for cement testing by API RP 10B-2 (2013).

Table 12 - Details of each sample set up

Rock	Pipe eccentricity	Additives	Number of samples
Sandstone	Concentric	Neat Class H	3
		Class H + 0.5% nano	2
		Geopolymer	2
		Class H + 10% mud	3
	Eccentric	Neat Class H	3
Shale	Concentric	Neat Class H	2
	Eccentric	Neat Class H	2

a) b)

Figure 18 - a) Blender used for cement slurry preparation and b) Thermo Scientific water bath for curing samples.

3.3. Digital Image Correlation under Indirect tensile stress testing conditions

Indirect (or splitting) tensile strength testing is recommended for cement mechanical testing according to API 10B-2 (2013) since failure of set cement in the wellbore will more likely be

tensile in nature because cement is much stronger in compression than it is in tension. There are various loads that are incurred by the cement sheath during the lifetime of the well which include the mechanical loads (pressure), chemical degradation and thermal stresses on the casing among others. This means that majority of the stresses on the hardened cement are propagated from the casing. In addition, there is hydraulic pressure from the subsurface formations and the fluids within their structures which apply stress perpendicular to the wellbore wall.

For this research, the Brazilian tensile equipment setup was used to apply a diametrical compression force on a cylindrical object. This meant that the load was applied at the formation side and there was no simulation of internal casing loads. This is a major deviation from ordinary oil well processes but it was incorporated for this research in order to have a baseline for experimentation of the cement bond integrity. The loading setup and equipment are shown in the **Figure 19**. The 2017 Instron 5982 series Universal Testing System with an incorporated load-control interface was used for this research. The maximum loading capacity is 100 kN with 1430 mm vertical test space (LabWrench (2017). The loading interface was calibrated to provide axial displacement accuracy to 0.1μm.

Figure 19 - Instron 5982 Universal Testing System

In this work, a software program called ARAMIS Professional®, produced by GOM Inspect, was used to create and analyze the strain field maps of the cement systems. Images were captured by a pair of ARAMIS Adjustable 12.0 megapixel monochromatic cameras with LED lighting and a laser pointer for optimum sensor adjustment. The cameras were equipped with a pair of Schneider 50 mm f/2.8 compact vision lenses. Images were captured and transferred to the software at a rate of 3 frames per second. Subsequently, the strain image maps were processed at the end of testing with the ARAMIS Professional® software. The sample test duration was less than 6min which corresponds to ASTM guidelines (2008). For this research, the applied frame rate was sufficient to provide detailed information on the evolution of failure as a function of the axial displacement.

According to ASTM D3967-08, the recommended length to diameter ratio of the cylindrical samples is 0.2 to 0.75 (ASTM 2008). The sample diameter must also be above ten times the largest

particle grain size of the sample. Failure of set cement in the wellbore will more likely be tensile in nature since cement is much stronger in compression than it is in tension.

The API recommended indirect tensile strength test is a viable method to determine the tensile strength of cement samples for better cement designs. There is concern about the effect of the high compressive stress at the platen point of contact with the samples. This has been averted by distributing the applied force along a small part of the surface circumference instead of a point force. The platens that were used have grooves to induce this effect on the samples (**Figure 20**).

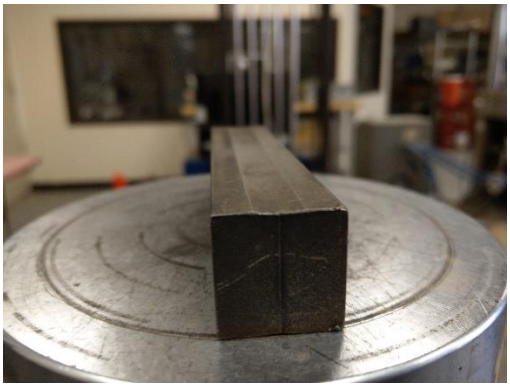

Figure 20 - Base platen with noticeable center axis groove.

Other methods include Direct Uniaxial Tensile strength (UTS) in which a tensile stress is induced on the specialized cement molds along the grip points between the samples and the platens as in the STS method (Bybee, 2004). The results of tensile strength from this test have been tested to be higher than those from the indirect tensile test because of the different phenomenon created by stress progression in the cement in the two methods.

On the other hand, Digital Image correlation (DIC) could be a more applicable tool for determining the deformation and strain fields across the surface of an object under stress. DIC method is a non-contact, real-time and flexible technique that measures any desired and exposed region of object

(Sutton et al. 2009). The theoretical fundamentals of the DIC technique were first introduced by Chu et al. (1985). This research has extended majorly into material testing and civil engineering industries and has only been introduced into geomechanics in the last 10 years (Sutton et al. 2000).

Particular research regarding the oil and gas industry has been majorly fracture propagation in reservoir rocks. Mokhtari et al. (2017) studied complex fracture propagation in naturally fractured Buda limestone under dynamic loading using DIC. This application of DIC in strain measurement over time showed fracture initiation and method of propagation in a heterogeneous sample until rock failure. Nath et al. (2017) investigated the effect of saturation and fracture patterns on the fracture development and the tensile strength of different sandstone and carbonate rock types. Using DIC, the research showed that there is a causal relationship between porosity, anisotropy and saturation with tensile strengths of the rock samples. This was in addition to observing and defining the strain development as the fractures formed and propagated.

Directly regarding cement-casing bonding, Nath et al. (2018) carried out preliminary tests to observe the strain development of Neat Class H samples bonded to steel. The cement either contained additives or was mud-contaminated. Using DIC, image maps clearly showed the compressive strain in the y-axis and tensile strain in the x-axis as a result of diametrical compression of the cement samples. It was observed that there was erratic deformation of 10% by volume mud-contaminated Neat H cement and rapid deterioration of the cement-steel bond (**Figure 22)** compared to Neat Class H samples (

Figure 21).

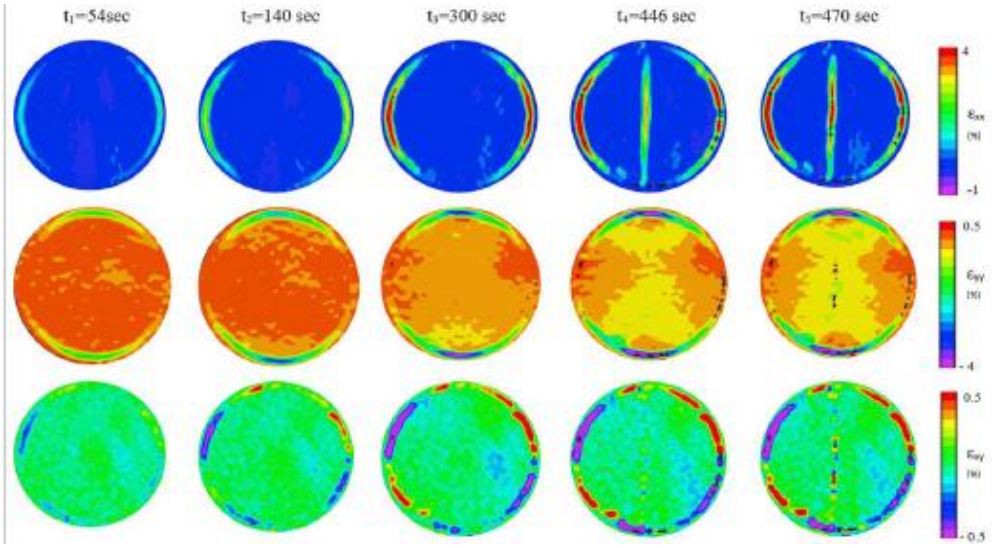

Figure 21 - Tensile, Compressive and shear strain development with time for Neat Class H cement with steel (Nath et al. 2018).

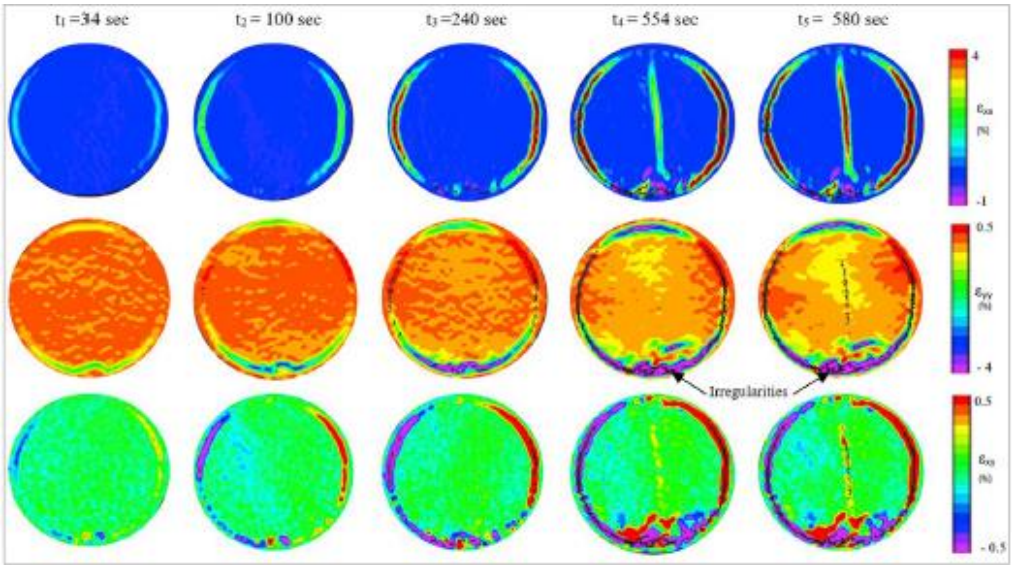

Figure 22 - Tensile, Compressive and shear strain development with time for Neat H 10% by volume mud-contaminated cement with steel (Nath et al. 2018).

For this research, the experimental procedure detailed in Nath et al. (2017) was used to achieve the test objectives as shown in **Figure 23.** It should be noted that the sample preparation ends with spray painting the face of the sample to be tested with a black and white speckled pattern as shown

in **Figure 24**. This is because during the Brazilian test, the DIC software tracked the displacement of the speckles as a result of the compressive load and measure displacement to calculate the strain along the surface of the sample. A more detailed instruction and explanation of the DIC principles are shown in **Appendix A**.

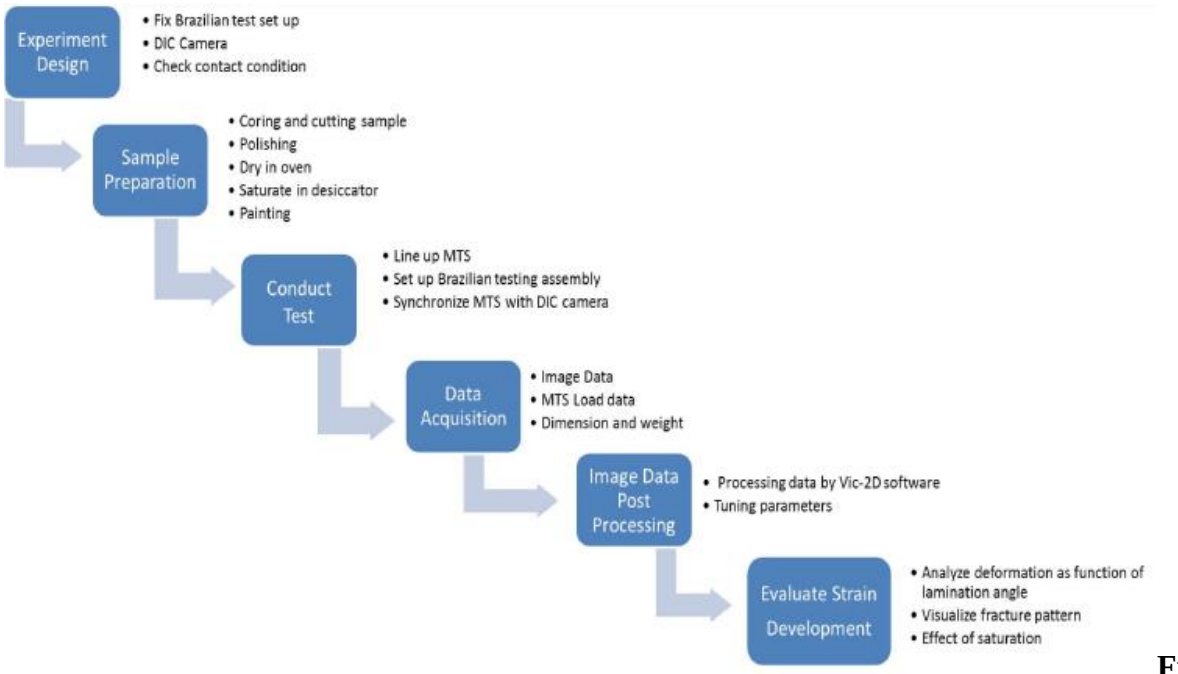

Figure 23 - Experimental procedure (Nath et al. 2017)

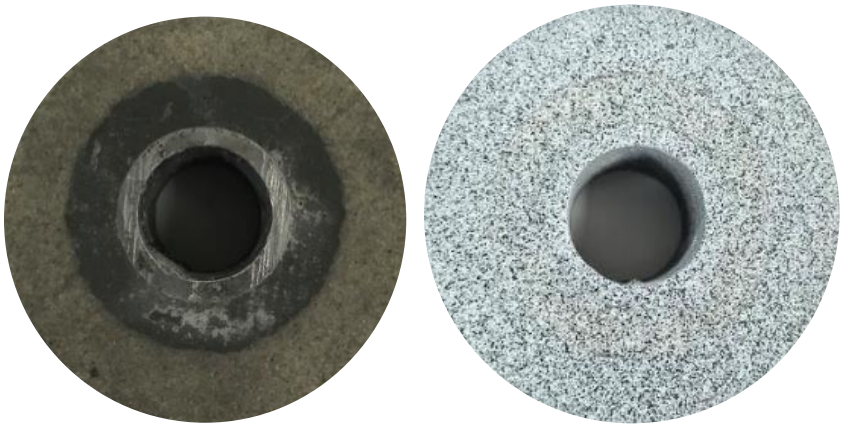

Figure 24 – Sample preparation before painting (left) and after painting (right)

The cameras were calibrated and synchronized with the load frame to achieve synchronized strain and load data at similar time steps. This non-contact optical technique allowed for processing of the images to provide strain image maps. While diametrically compressing the platens at a rate of 0.1 mm/min, the load frame was programmed to record compression data every tenth of a second. The LED lights were set up and calibrated critically to measure the speckle paint pattern on the cylindrical samples was correctly identified by the cameras (**Figure 25)**. The displacement error is 0.01 pixels by theoretical analysis and the accuracy was to 1 μm based on our calibration. The camera recorded photographs at the 3 frames per second (fps) because of the limitation of the photogrammetry software to only record a maximum of 2000 frames.

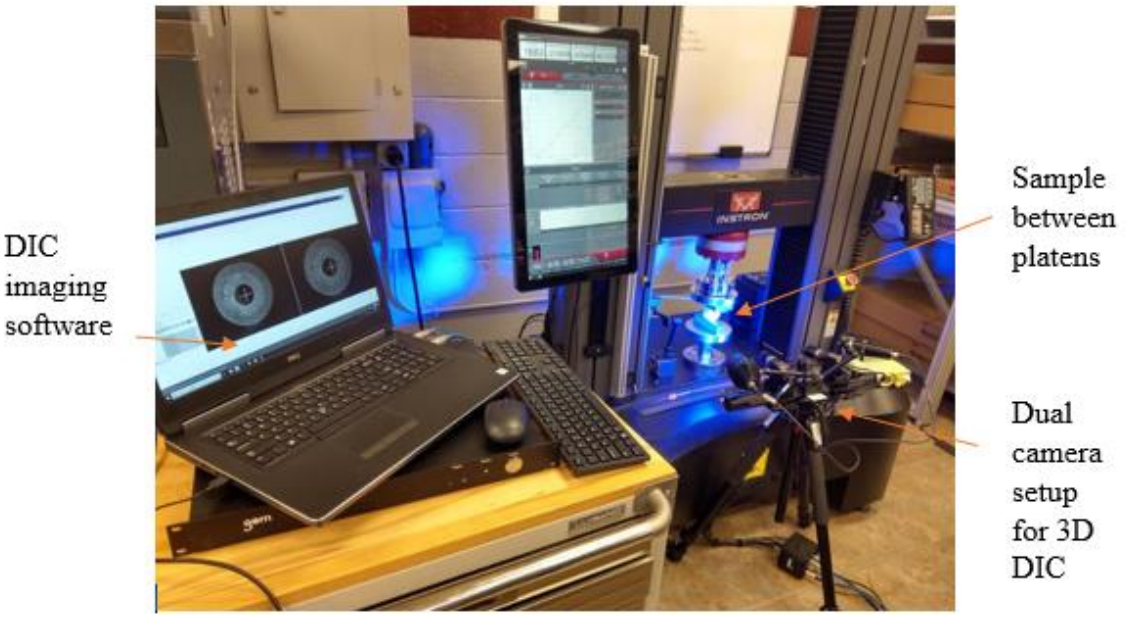

Figure 25 - Experimental set up showing ARAMIS 3D DIC camera with software linked to loading platform

During this testing, the number of captured number of images varied from 1100 to 1600 for the tested samples. Once the test was completed, the images were analyzed using digital image correlation to evaluate tensile and compressive strain as shown in **Figure 26**. In the figure, the

compression load is applied diametrically and the compressive strain is generated in the y direction while the tensile strain is generated in the x direction. The positive values on the strain scale are tensile while the negative values are compressive strain in terms of percentage (%). This would provide sufficient information on the strain development and formation of radial fractures in the cement, as well as, degradation of the interfacial bond between the casing (pipe) and cement.

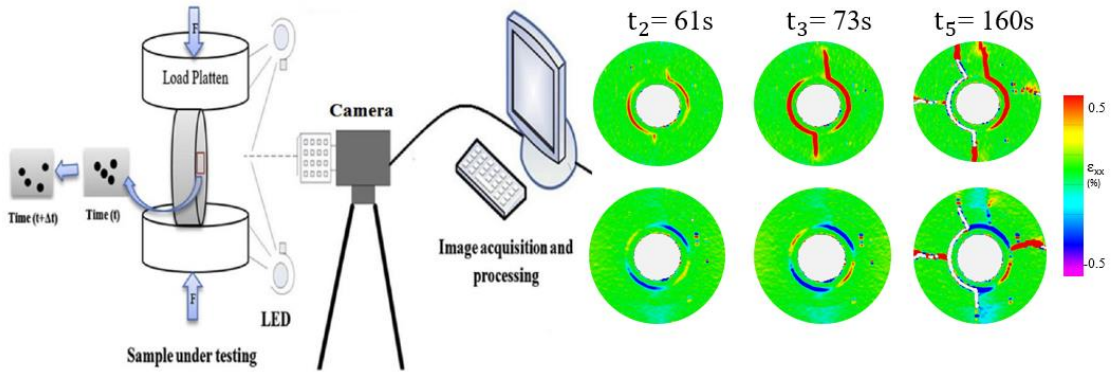

Figure 26 – Schematic of the sample loading and the DIC software strain mapping

3.4. Microscope imaging

Two samples for each difference sample configuration (except for eccentricity) were prepared, cured for 24 hours under elevated temperature (70^{o}C) conditions before transferring them for microscope imaging. The microscope imaging was done at 20x magnification specifically to provide information of the bond between the cements and the steel or formation interface using a Laser microscope (**Figure 27)**.

The accuracy of the images taken using the Keyence VK-X200 series laser microscope was 0.01μm with images taken using the 10x, 50x and 200x in order to capture the most definitive images. Microscope imaging was a significant part of this research methodology to show the

formulation of the cement bonds with the two substrate surfaces. This would also complement the information derived from the strain image data.

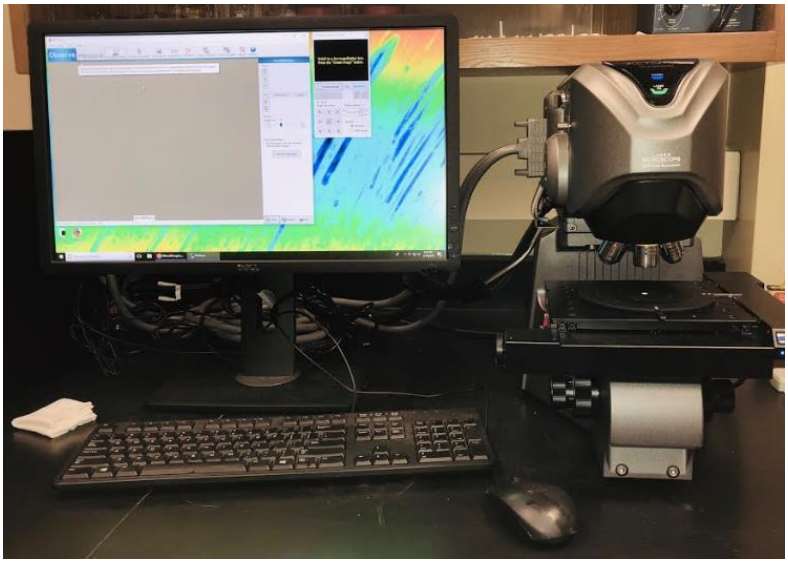

Figure 27 - Keyence Laser microscope for microscope imaging.

4. Results

This section provides results from the strain development maps and discussion of these results using microscope images. The load-control system provided real-time measurements of the load applied and the vertical displacement with time. The strain was calculated as the ratio of vertical displacement to the original length of the sample (2 inches). With this information, the load-strain plots were generated for each sample. Using the DIC software, strain image maps were constructed to correlate with the different aspects shown in the load-strain plots. It should be noted that the slope of the load-strain curves will increase gradually since these are not isotropic samples but a combination of three different materials with different mechanical properties.

The strain maps include the horizontal/tensile (ε_{xx}) and vertical/compressive (ε_{yy}) strain of the samples from initiation to sample failure under stress. This study is based on the culmination of strain development throughout sample deformation to define interfacial bond integrity as a function of the quantified deformation under the indirect tensile load. The various microscope images taken at different points of the interface between the three cement systems and formation/steel are displayed in **Appendix B**.

4.1. Effect of lithological aspects

As mentioned in Section 3, two lithologies were cored and used for these tests: Berea sandstone and Mancos shale. The effect of the inner substrate roughness, porosity and grain size on the development and strength of the cement bond was vital in the strain development during the diametrical compressive testing.

4.1.1. Digital Image Correlation

The base case for these experiments was Neat Class H cement placed in a concentric annulus between steel and sandstone. This was compared to the same system but with shale as the formation. The load-axial strain graphs for the two sample systems is shown in **Figure 30.** The nature of the two systems differs in that the vertical and horizontal strain occurs initially at the cement-steel interface (**Figure 28)** while the initial strain in the shale sample occurs at the cement-shale interface (**Figure 29)**. There is no strain development along the cement-sandstone interface throughout the test.

There is also evidently a difference in the nature of the load-strain curves of the two samples. There are a few more drops in the load as the strain is developed along the cement-shale interface (**Figure 30**). Since the loading data acquisition for axial displacement is accurate to 1μm, the erratic curve progression in the shale system has been attributed to a slipping effect at the interface between cement and shale.

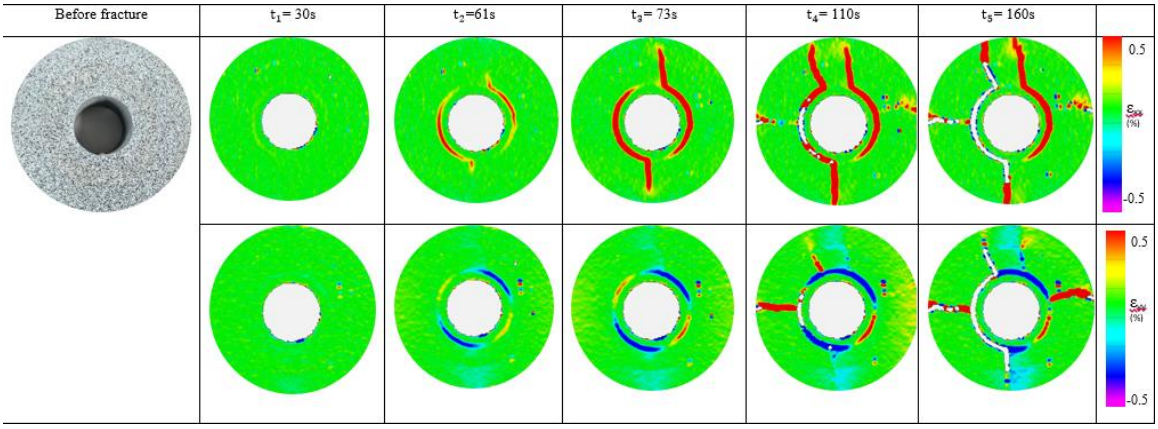

Figure 28 – Strain development (ε_{xx} and ε_{yy}) for Sandstone Neat H concentric system

Strain development at the cement-steel interface in the shale samples occurs at a later time (than in the sandstone samples) before the point of sample failure. This also differs to the sandstone

system in that the sample fails after radial fractures propagate parallel to applied force from the cement-steel interface through the cement and finally through the sandstone layers. In the shale system, under the loading stress, the fracture propagates from the cement-shale interface 90^{o} to the applied force. The microscope image results give an insight as to the bonding dynamics that could explain this phenomenon.

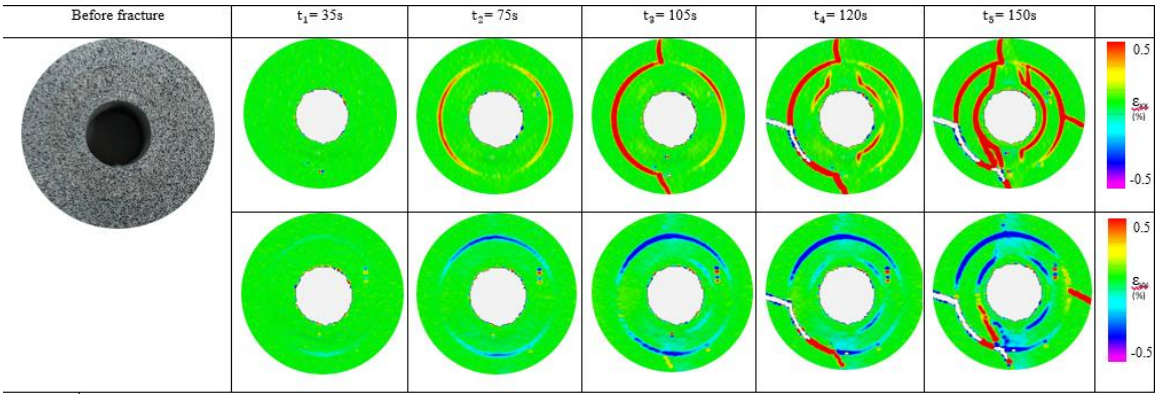

Figure 29 – Strain development (ε_{xx} and ε_{yy}) for Shale Neat H concentric system

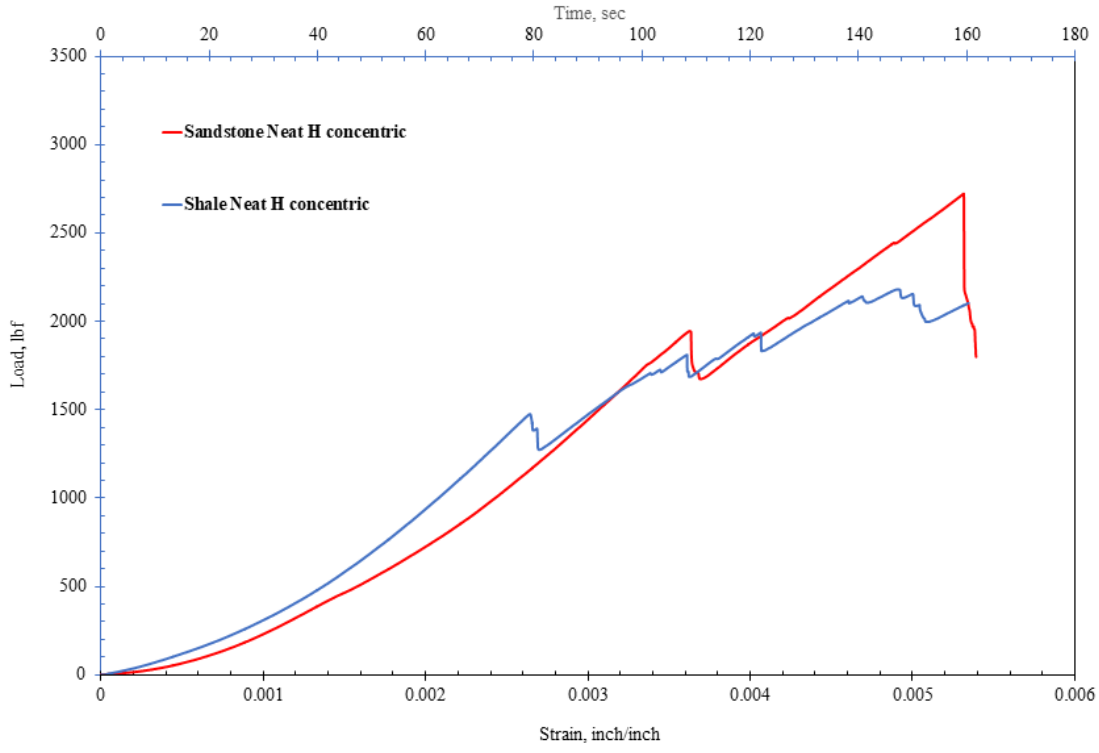

Figure 30 – Load vs. axial strain of Neat H cement in concentric sandstone and shale systems

4.1.2. Microscope Imaging

The images of the hydraulic bond with sandstone showed complete bonding at interface with no visible distinction of interface boundary. The mechanical interlocking of the cement into the crevices of the sandstone surface as a result of the cement flowing into the void spaces and grooves of the substrate surface was visible (**Figure 31**). This created a clearly mechanical interlocking bond that would require a higher shear force to disintegrate.

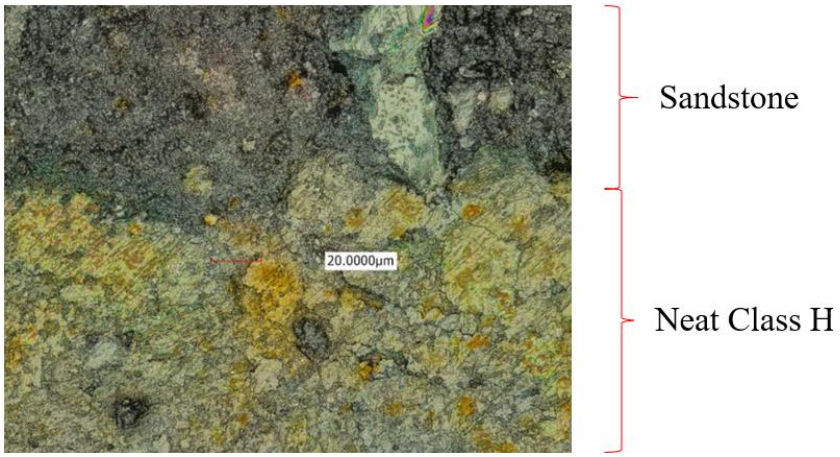

Figure 31 – Microscope image of the interfacial bond between Neat Class H cement and sandstone

The microscope images of the bond between Neat Class H and shale showed a smooth (almost continuous) interfacial bond (Figure 12). The shale inner surface is evidently smoother with less porosity (surface pores) and permeability than sandstone (**Figure 32**). Mudstones such as Mancos shale have particle sizes ranging between 10 – 50 micrometers with mud filling the pores within the structure (Li and Schieber 2018). For comparison, the particle size in Berea sandstone vary between 150 – 300 micrometers and a lightly cemented porosity above 23% (Churcher et al. 1991).Therefore, even with evidence that the cement wetted the surface of the shale creating a

visible bond, there is no interlocking at the interface. This means the shearing force to displace the cement sheath in this case will be much lower than with sandstone.

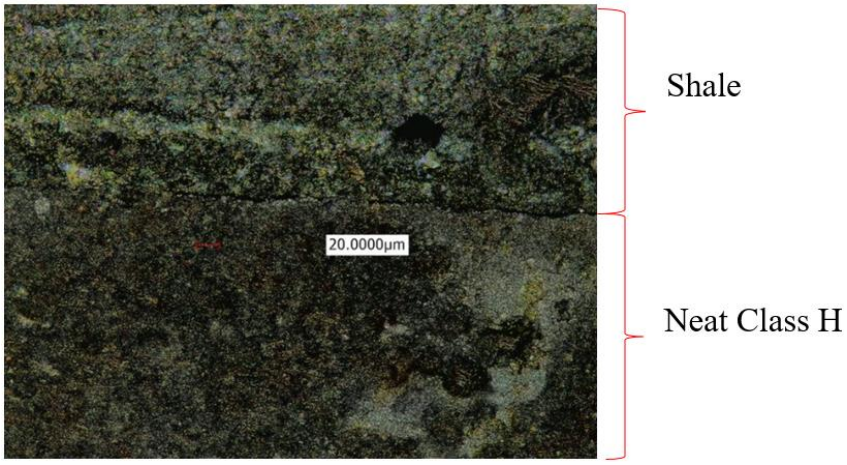

Figure 32 - Microscope image of the interfacial bond between Neat Class H cement and Mancos shale

4.2. Effect of mud contamination

As earlier on stated, mud contamination critically reduces the compressive and tensile strength of the cement as it is being placed in the annulus which has been correlated with negatively affecting the bond strength. These results show the detrimental effect of a poor bond as a result of mud contamination.

4.2.1. Digital Image Correlation

From **Figure 33**, it is evident that the strain development and progression of the mud-contaminated Neat H sample is very similar to the base case Neat Class H system (**Figure 28**). The strain initiates at the cement-steel interface and results in the formation of a radial fracture which propagates through the cement and the sandstone finally leading to sample failure. The effect of mud contamination of cement is shown in the load-strain curves (**Figure 34**). Firstly, at every time step during which strain or fracture was developed in the system, there is a slipping effect shown in the

graph. The more evident difference is that the load required to cause disintegration of the bond between mud-contaminated cement and steel (640 lbf) is more than 4 times less than that in the Neat Class H system (2740 lbf). The sample (shear bond) fails slightly later (45 seconds) because the mud-contaminated cement will have a much lower compressive strength and as a result will deform slightly more than Neat Class H.

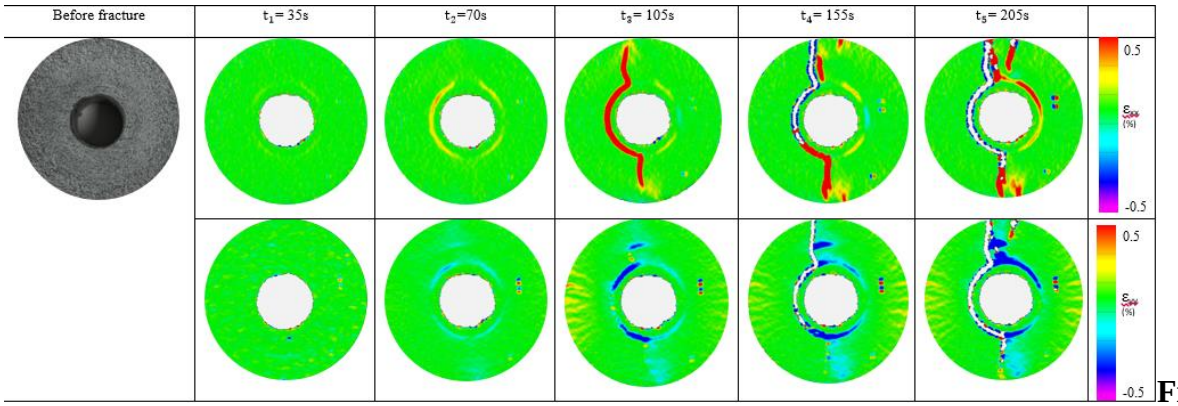

Figure 33 – Strain development (ε_{xx} and ε_{yy}) for Sandstone mud-contaminated H concentric system

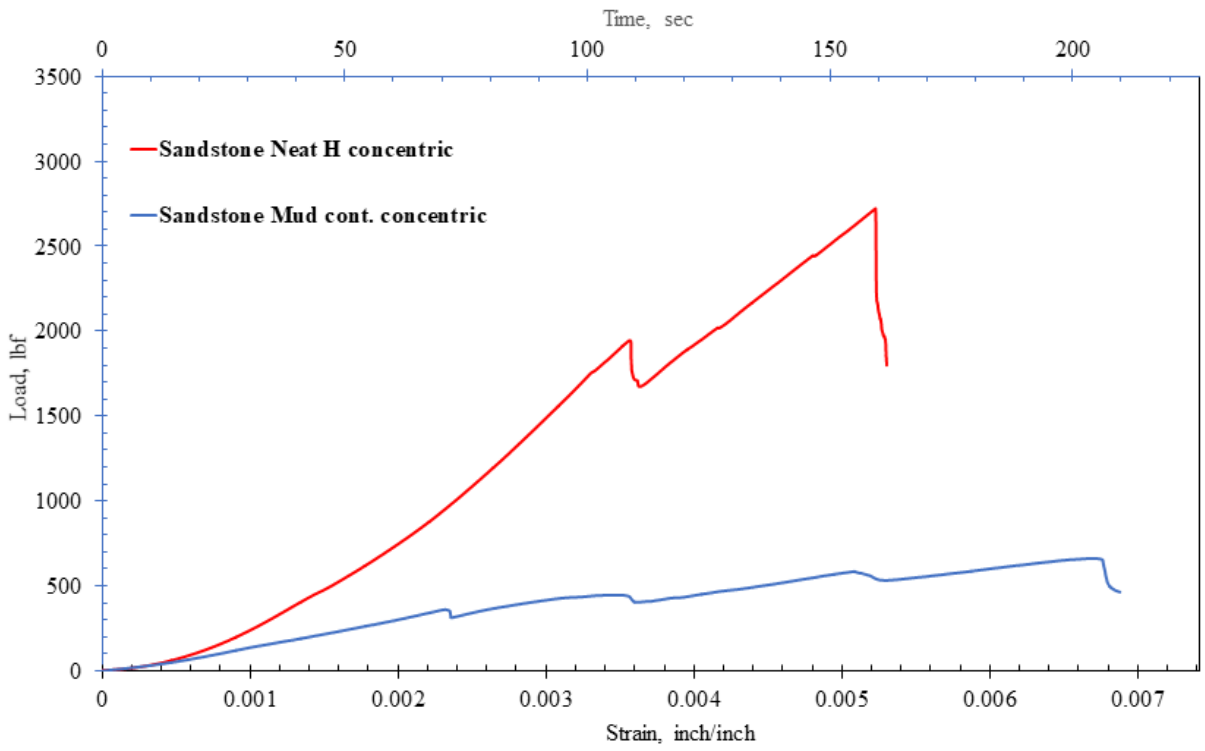

Figure 34 – Load vs. axial strain of effect of mud contamination in concentric sandstone systems

4.2.2. Microscope Imaging

The images of the hydraulic bond with sandstone are similar with in the case of Neat Class H. The images showed complete interlock bonding at the interface at some locations but gaps at other locations of the interface boundary (**Figure 35**). The imaging of the cement bond with steel showed that there were regions of the interface where the cement did not have any contact with the steel leading to no actual bond being formed (**Figure 36**). This is because the mud layer on the steel prevented the flow of the cement into the substrate surface of the steel preventing the formation of a bond. This would correlate with the slipping effect seen in the load-strain curve during deformation.

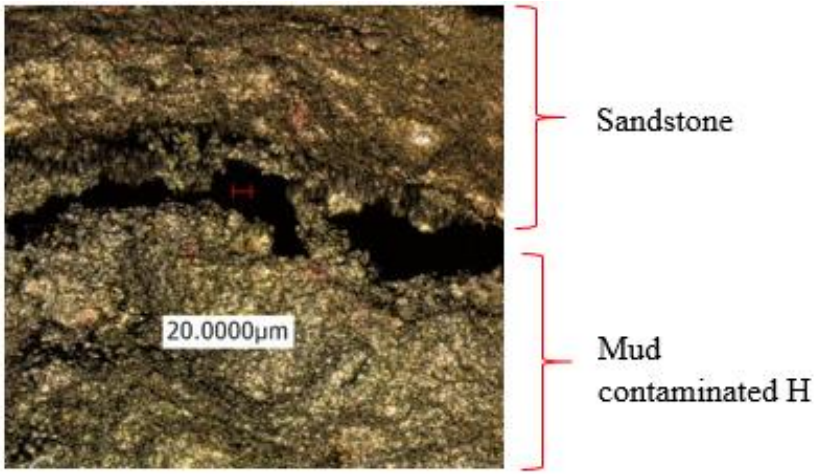

Figure 35 – Microscope image of the gap between mud-contaminated H cement and sandstone

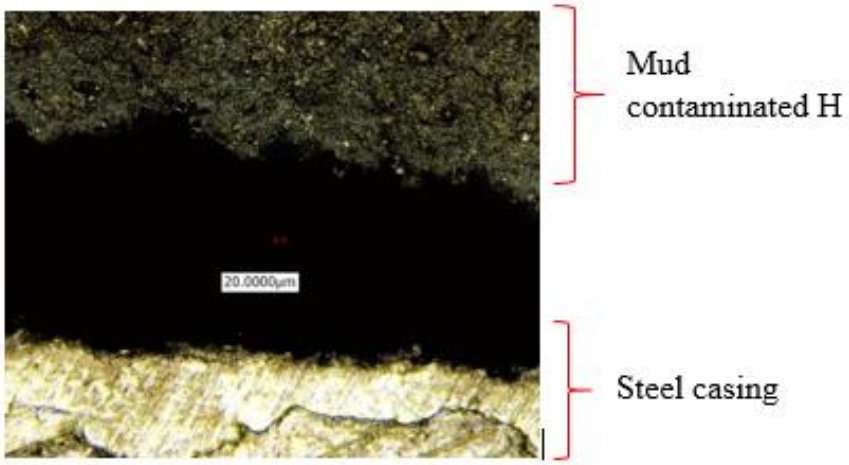

Figure 36 – Microscope image of the gap between mud-contaminated H cement and steel

4.3. Effect of eccentricity

Casing eccentricity is one of the issues that can be controlled by increasing the use of centralizers. This is a major issue that leads to remedial cementing jobs because the cement bond collapses much earlier than in near-concentric systems. The results reveal this situation in detail.

4.3.1. Digital Image Correlation

For the eccentric in sandstone case, the tensile strain initiates along the cement-steel interface very similar to the concentric case. The compressive strain initiates and develops at the upper cement-steel interface in addition to the cement-sandstone interface closer to the lower platen (**Figure 37**). The tensile strain builds and leads to the formation of the radial fractures that propagate in the direction parallel to the loading of the sample. The sample fails with the disintegration of the shear bond similar to the concentric case. The load-strain curve for the eccentric case show similar trend to the mud-contaminated case. The maximum load before the failure of the shear bond in the eccentric case (1100 lbf) is 2.5 times less than that for the eccentric case (2740 lbf) as shown in **Figure 38**.

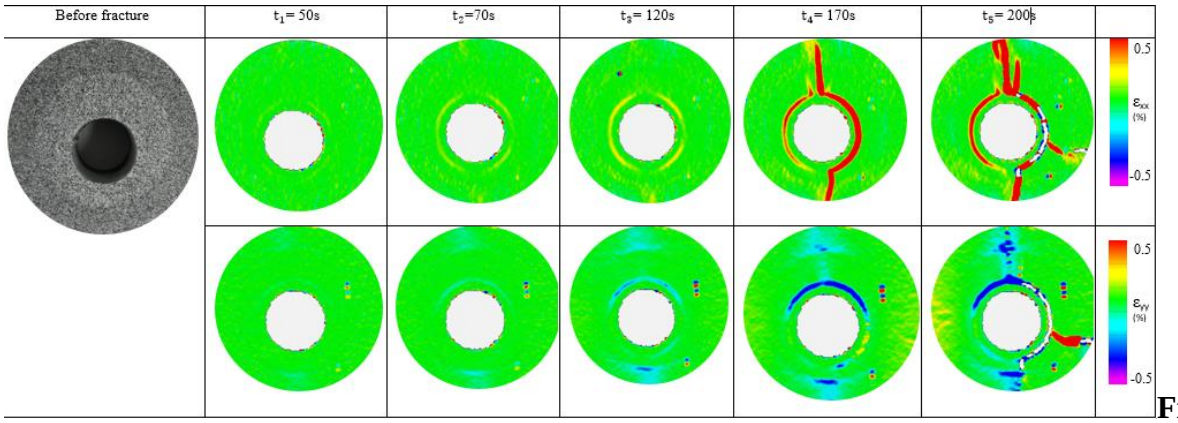

Figure 37 – Strain development (ε_{xx} and ε_{yy}) for Sandstone Neat H eccentric system

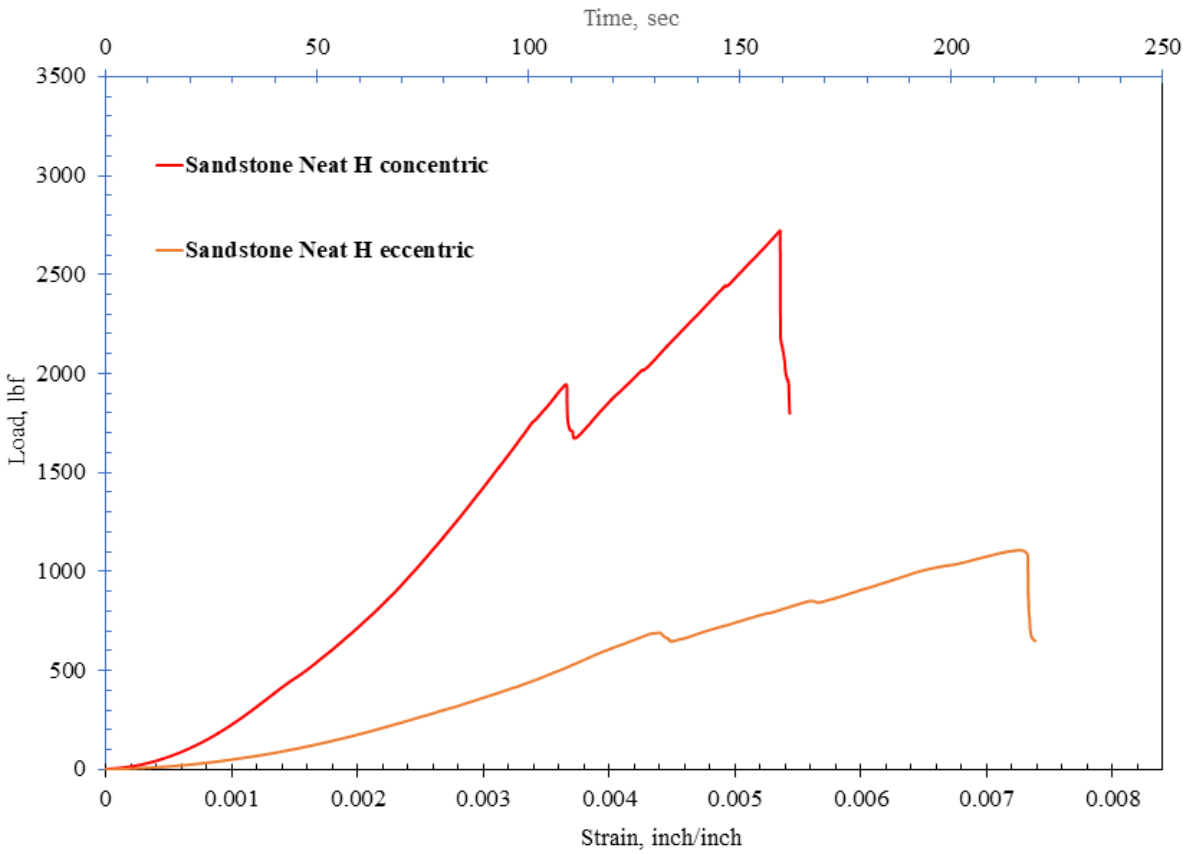

Figure 38 – Load vs. axial strain of Neat H cement in concentric and eccentric sandstone systems

The effect of eccentricity in shale samples differed in terms of strain development to the sandstone samples. The compressive and tensile strain initiated along the cement-shale interface (**Figure 39**) as in the concentric case **(Figure 29).** Specifically for the concentric case, there was evidently strain development at the cement-steel interface as the load increased. Radial fractures were then developed from both interfaces parallel to the loading direction before both the hydraulic and shear bonds were disintegrated. The load-strain curve showed that it required a less load (1350 lbf) in the eccentric case to cause sample failure than in the concentric case (2300 lbf) in the same duration of loading (

Figure 40). The curves for the shale cases showed that there was a number of slips along the bonding interfaces during strain deformation of the samples compared to the sandstone samples.

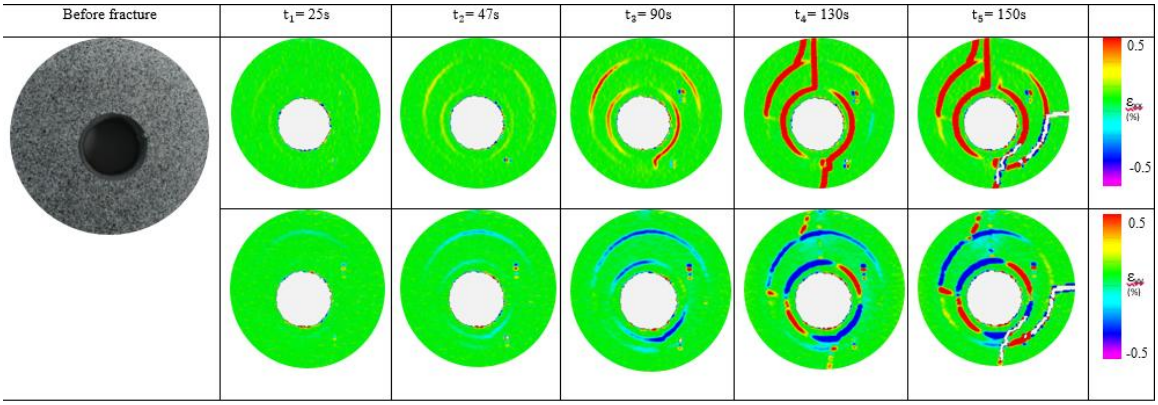

Figure 39 – Strain development (ε_{xx} and ε_{yy}) for Shale Neat H eccentric system

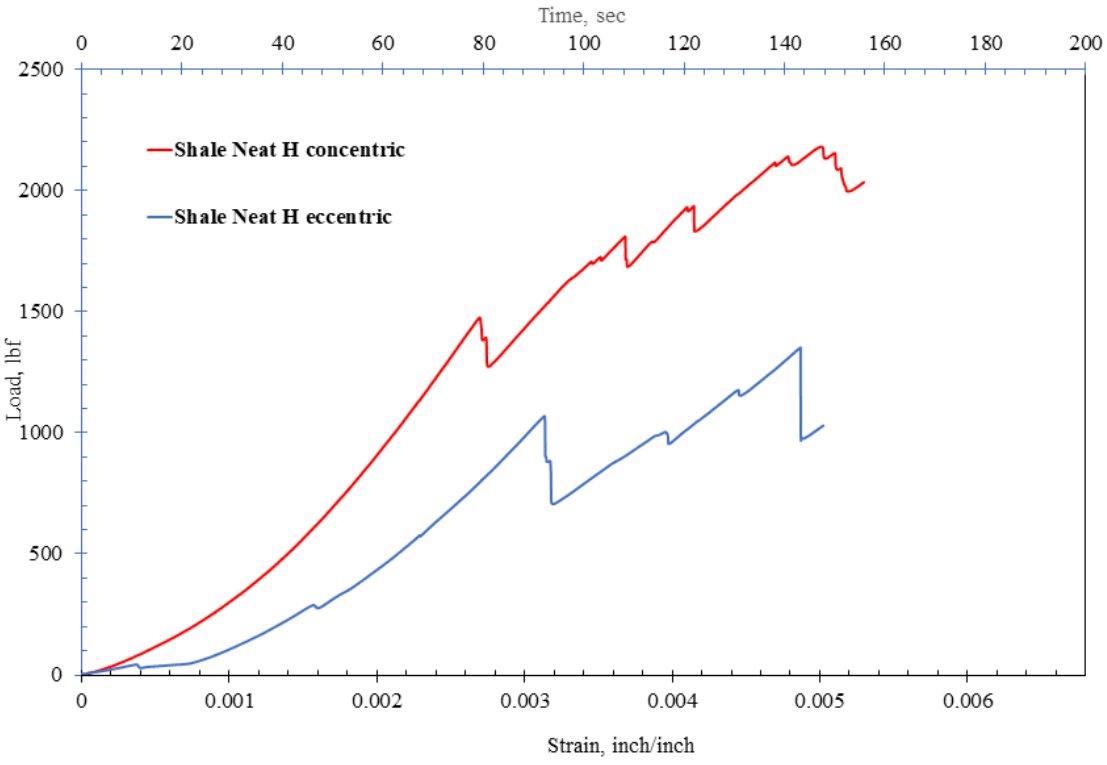

Figure 40 – Load vs. axial strain of Neat H cement in concentric and eccentric shale systems

4.4. Addition of nano-synthetic graphite

There has been increased research into the use of nano-silica and other nano-particles integrated into Portland cement with the purpose of reducing the effect of high temperatures on the flow and mechanical characteristics of the cement. These results reveal the advantage of nano-modified cement with regards to bonding dynamics.

4.4.1. Digital Image Correlation

Firstly, it took twice as long to initiate compressive and tensile strain (130 seconds) in the nano-modified cement system (

Figure 41) compared to Neat Class H system (61 seconds). The progression of strain development was similar to that in the Neat H case with the increase in strain along the cement-steel interface before formation of the radial fracture progressing parallel to the loading direction. **Figure 42** shows the load-strain behavior of the nano-modified Class H cement compared to Neat Class H. The plot shows that there was prolonged deformation of the nano-modified cement in the system before complete shearing of the cement bond with steel. It took more than twice as long before sample failure (350 seconds) compared to Neat Class H case (160 seconds) under the constant vertical loading displacement.

This would mean that the nano-modified cement (after 24 hours of curing) was more ductile since it deformed much more than the brittle Neat Class H before sample failure. It can be speculated that it would require more operational loading on the casing before the radial fractures are formed and the shear bond is affected as compared to the Neat Class H.

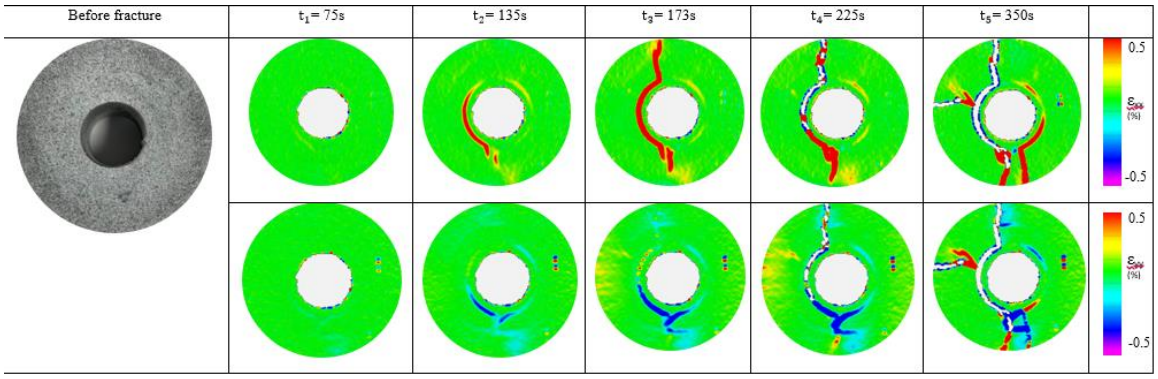

Figure 41 – Strain development (ε_{xx} and ε_{yy}) for Sandstone Nano-modified H concentric system

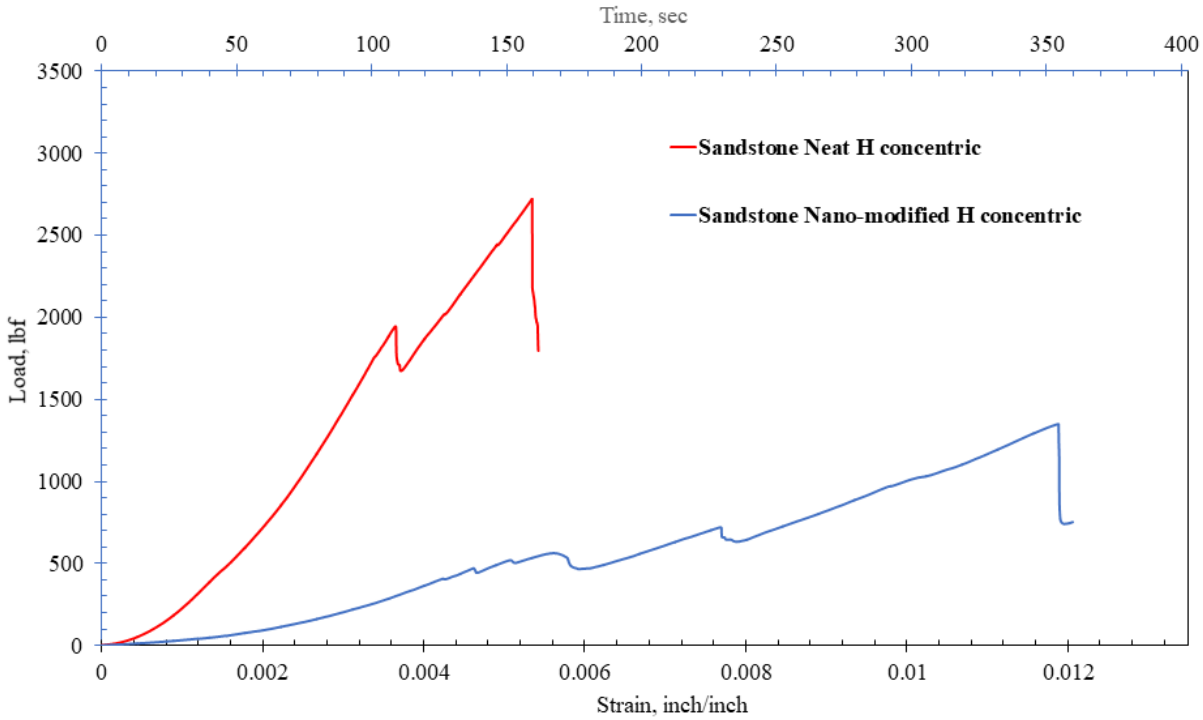

Figure 42 – Load vs. axial strain of effect of nano-modification of Class H in concentric sandstone systems

4.4.2. Microscope Imaging

The microscope images of nano-modified cement with sandstone and steel are similar to those of Neat Class H. There was a mechanical interlocking bond formed with both the steel pipe (

Figure 44) and the sandstone (**Figure 43**) surfaces with the effect of porosity at the sandstone substrate surface encouraging the formation of a more complete bond. The microscope images

only gave an insight to the formation of a good bond but not the strength or the brittleness of the cement.

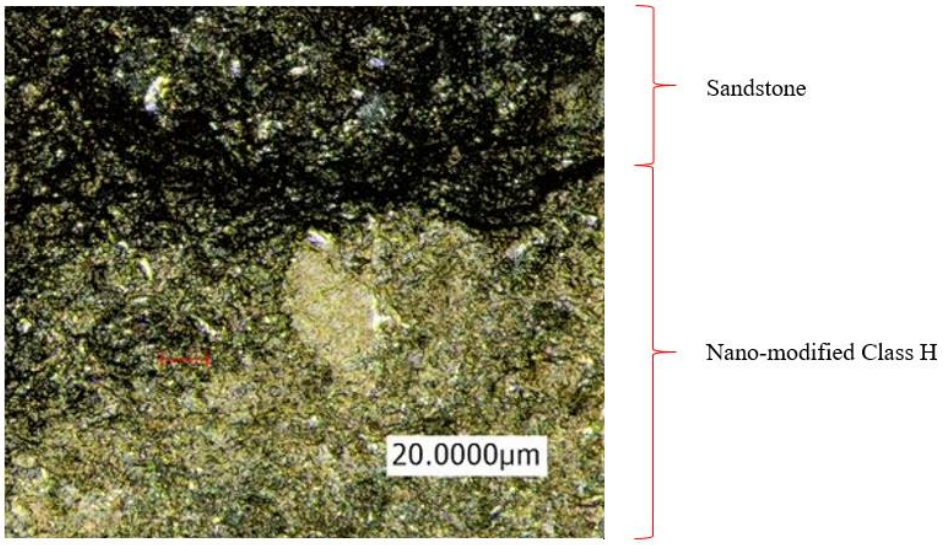

Figure 43 – Microscope image of the interfacial bond between nano-modified H cement and sandstone

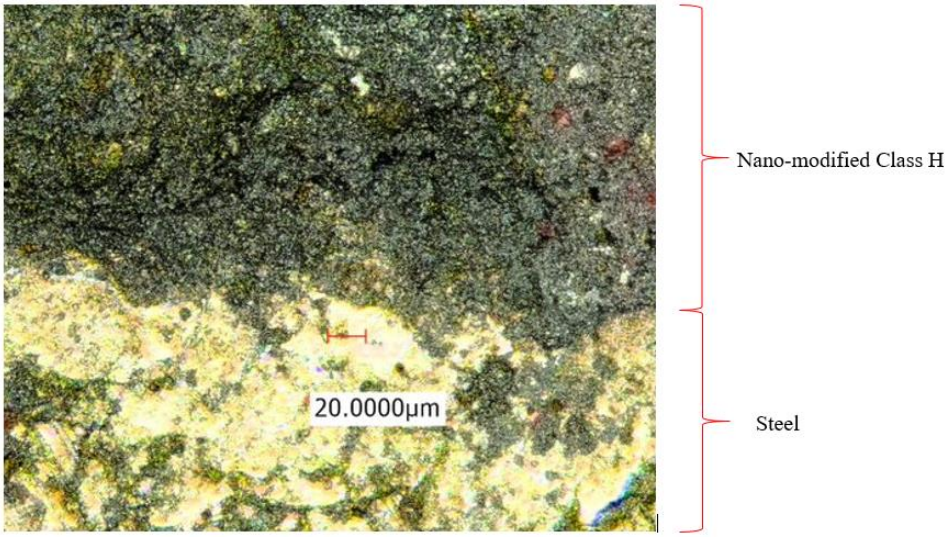

Figure 44 – Microscope image of the interfacial bond between nano-modified H cement and steel

4.5. Geopolymer cement

As a new binding material hoped to replace Ordinary Portland cement, geopolymers must have a certain mechanical and bonding characteristics. The results give an insight to how advantageous it would be to use geopolymers as a cementing system in oil and gas wells.

4.5.1. Digital Image Correlation

The strain deformation for this sample of the geopolymer case was very similar to that in the Neat Class H system. Strain initiated along the cement-steel interface and developed leading to the formation of radial fractures and finally sample failure (

Figure 45). With the same vertical displacement of the loading system over time, the duration before disintegration of the shear bond as a result of sample failure (250 seconds) was longer than that of Neat Class H system (**Figure 46**). There was visually continuous deformation throughout the loading process from the image maps with strain occurring within the cement itself. There is also less load recorded until shear bond failure.

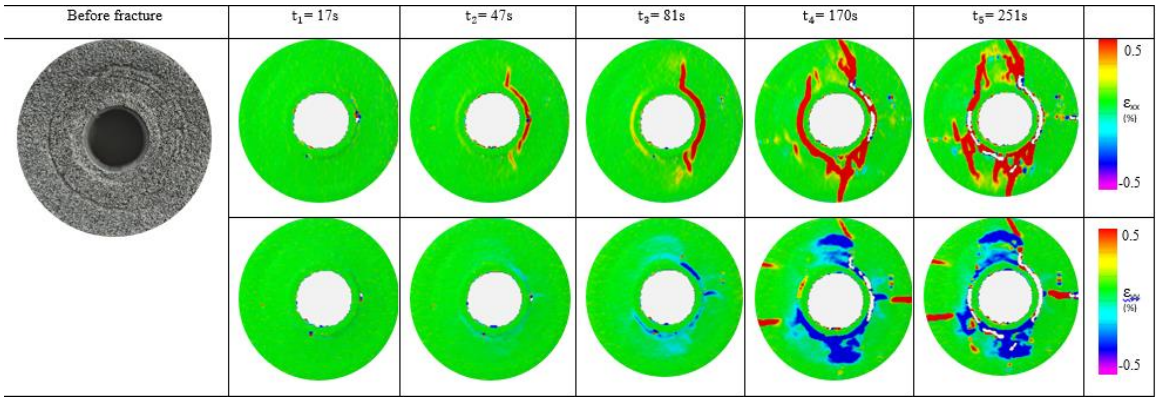

Figure 45 – Strain development (ε_{xx} and ε_{yy}) for Sandstone geopolymer concentric system

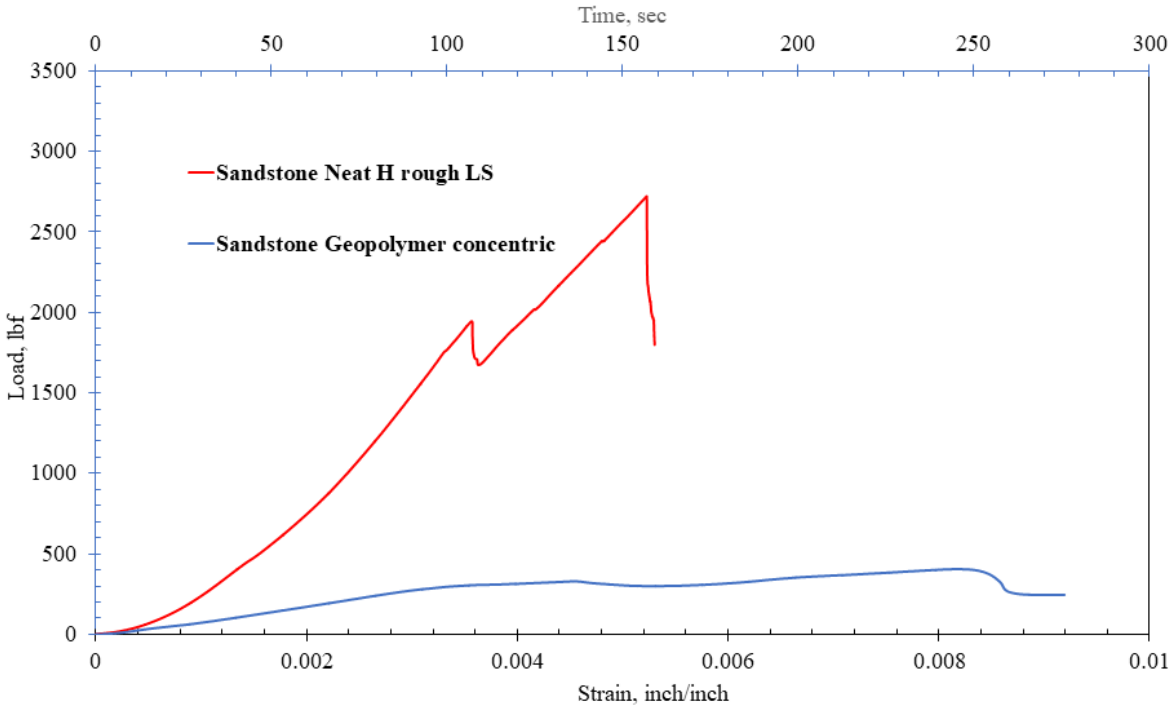

Figure 46 – Load vs. axial strain of geopolymer cement vs. Neat Class H in concentric sandstone systems

4.5.2. Microscope imaging

The microscope imaging of the geopolymer bonding with sandstone revealed that the geopolymerized cement wetted the surface of the sandstone throughout the curing like in the case with Neat Class H. The laser microscope images showed that the cement flowed into the void spaces and displaced the air trapped in those crevices in order to create the interlocking mechanical bond (**Figure 47)**. In these images, the quartz crystals in the sandstone will differentiate the two subtrates.

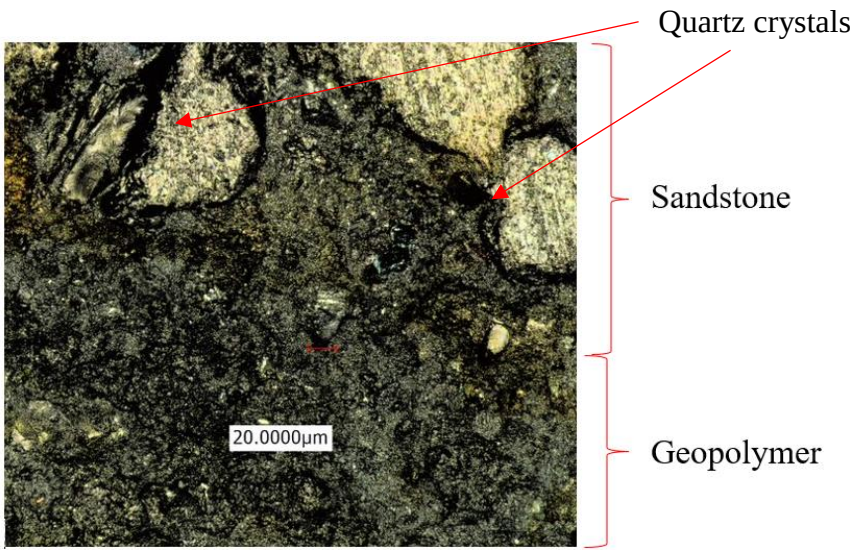

Figure 47 - Microscope image of the interfacial bond between geopolymer cement and sandstone

In addition, there was evidence of a good shear bond of the geopolymer cement with steel as shown in

Figure 48. Similar to the case with Neat Class H, the geopolymerized cement wetted the surface of steel allowing for the formation of a complete mechanical bond. Evidently, the assumed shear force required to overcome the friction at the interface between cement and rough pipe will be higher than that with smooth pipe.

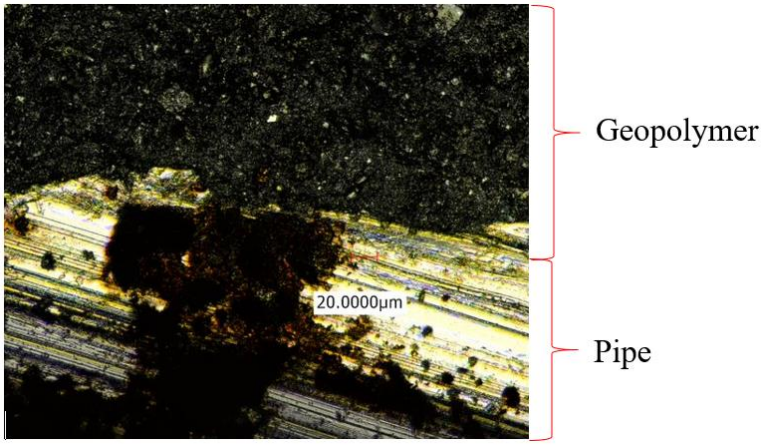

Figure 48 - Microscope image of the interfacial bond between geopolymer cement and steel

4.6. Unconfined Compressive strength (UCS)

The three different cement recipes were cured under water at a temperature of 70°C ± 5°C (158°F ± 9°F) and their unconfined compressive strengths were tested as well. Three samples were prepared for each of the cement systems and for each curing time. The cement curing durations tested were 24 hours and 7 days. From **Figure 49** there is a clear increase in UCS with curing time. Geopolymer cement acquired a 44% lower UCS (10.3 MPa) after 24 hours than Neat Class H cement (18.6 MPa).

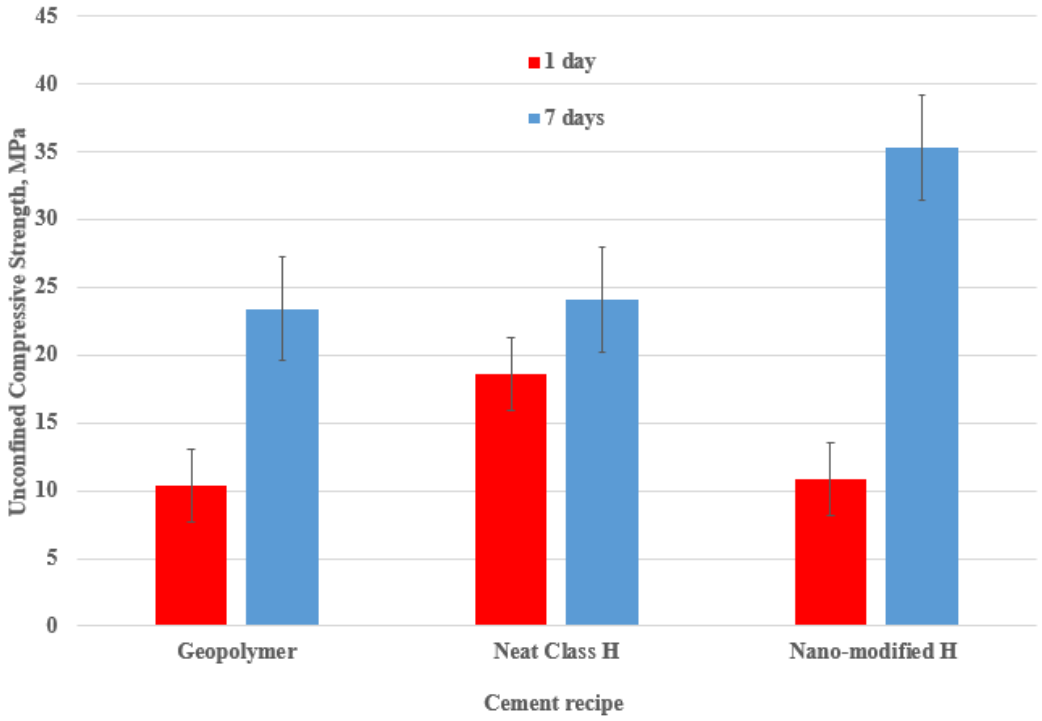

Figure 49 – Comparison of Unconfined Compressive strength for three cement recipes

On the other hand, nano-modified Class H cement had a 41.5% lower UCS (10.8 MPa) than Neat Class H. UCS is only one of the cement properties that are required for a viable oil well cement in addition to bonding dynamics and flow behavior under different subsurface conditions. Based on

these results it is evident that geopolymer cements should be field-tested and nano-synthetic graphite should be integrated in Portland cement designs.

4.7. Summary of DIC results

4.7.1. Axial load and axial strain to define deformation

Maximum load and Maximum axial displacement/strain before sample/shear bond failure, in combination, give us information about the deformation of the cement system as a generic sample configuration. **Figure 50** show the comparison of maximum load and maximum axial strain for all the tested sample systems.

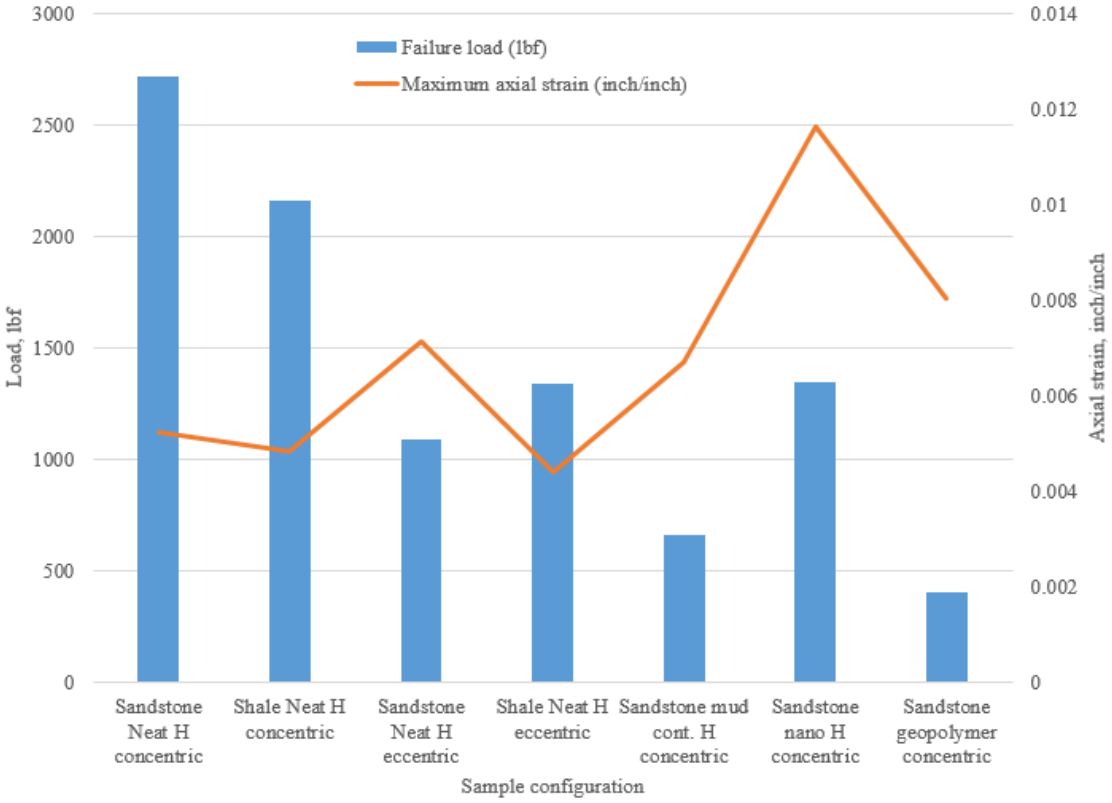

Figure 50 – Maximum load and axial strain before sample/interfacial bond failure

With regard to lithological aspects, the shale sample failure occurred along the cement-shale interface while the failure in the sandstone samples occurred along the cement-steel interface. For the concentric cases, it required 20.6% less load with 7% less deformation to lead to sample failure for shale than in sandstone. The strain initiated at the cement-shale interface and the cement-steel interface was also affected as well as deformation progressed. This means that the deformation of the cement sheath is more detrimental in Mancos shale reservoirs increasing the possibility for fluid influx from the formation due to cement debonding.

Regarding the detrimental effect of casing eccentricity, with only 37% increase in strain deformation, there was a 60% decrease in the maximum load for before shear bond failure for Neat H in sandstone samples. There is a recorded 38% decrease in load before failure for the eccentric case of the Neat H in shale for the same amount of axial deformation. Casing eccentricity can be reduced tremendously using more centralizers but a balance should be met to prevent stuck pipe due to high frictional load on the casing.

Regarding mud-contamination, there was a notable 75.7% decrease in the load required to fail the mud-contaminated H sample system even though there was a recorded 28% higher axial deformation. Mud contamination critically reduces the tensile and bonding strength of any cement system and research into preventing this situation should be taken into all cement designs with high precision.

Geopolymer and nano-modified Class H cements were chosen for testing because of the good mechanical properties (compressive and shear bond strength) in particular subsurface environments such as high pressure/high temperature (HPHT). According to Jafariesfad et al. (2017), a cement with lower Young's modulus and undergoes larger deformation (higher Poisson's ratio) is recommended to prevent cement sheath failure. **Figure 49** shows that both of these cement

recipes have lower compressive strength than Neat Class H cement after 24 hours. This correlates with the lower values of the maximum load that was required to fail the samples with nano-modified cement (38% less) and geopolymer cement (63% less). The effect of curing time will show an increase the compressive strength (and Young's modulus) of both cement systems and the load-strain curves will change significantly.

4.7.2. Specific failure energy

A combination of maximum load and maximum axial strain was used to calculate energy/work done per unit volume before sample failure as in **Equations 5, 6 and 7**. This is similar to the fracture and toughness energy defined by Barton (1982). Since all the samples had the same dimensions, the specific energy to fail the individual samples was plotted for comparison (**Figure 51**). The nano-modified H cement system required 10% higher specific failure energy as compared to Neat Class H cement system.

$$\sigma = \frac{F\ (lbf)}{A\ (in\text{^}2)} \quad \text{..... (5)}$$

$$\varepsilon = \frac{\Delta L\ (inch)}{L\ (inch)} \quad \text{..... .(6)}$$

$$\sigma * \varepsilon = \frac{F\ (lbf)}{A\ (in^2)} * \frac{\Delta L\ (inch)}{L\ (inch)} = \frac{Energy}{Volume} \quad \text{.....(7)}$$

On the other hand, even with a 53.8% higher maximum axial deformation, the geopolymer cement system required 77% less specific failure energy. This is because the cement system has not yet reached its maximum compressive strength since the cement samples were cured for 24 hours before testing. Geopolymer cements should continue to be an area of interest and bonding dynamics should be tested at different curing times and higher temperatures. The durability of

geopolymer cements has already been tested (Salehi et al. 2016b; Khalifeh et al 2017a) but further research is required.

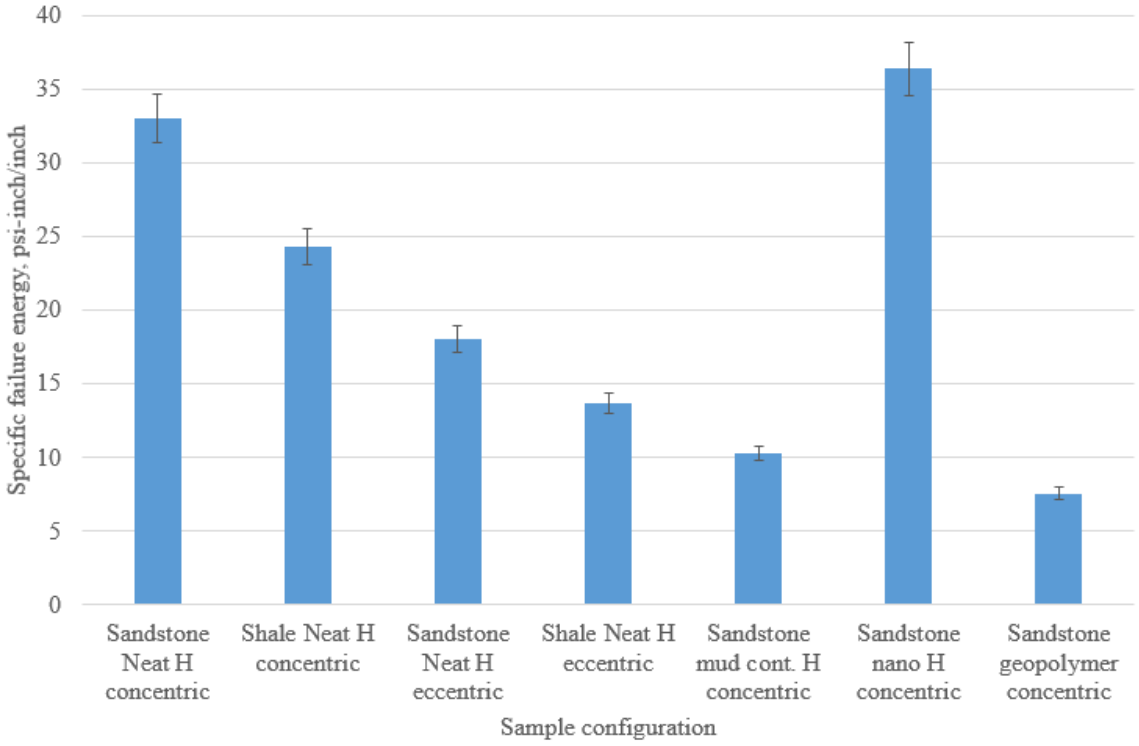

Figure 51 – Specific failure energy for each sample configuration

4.7.3. Sample Young's Modulus

Since the sample configuration is not isotropic (three different materials with different mechanical properties), the calculation of the Young's modulus (**Equation 8**) is to show the relative difference in the deformation characteristics of the samples under loading. Figure shows the comparison of the young's modulus for each cement system.

$$\sigma = E * \varepsilon \rightarrow E = \frac{\sigma}{\varepsilon} \quad \text{.....(8)}$$

σ is the maximum stress the sample incurred before sample failure;

ε is the maximum axial strain;

E is the sample Young's modulus.

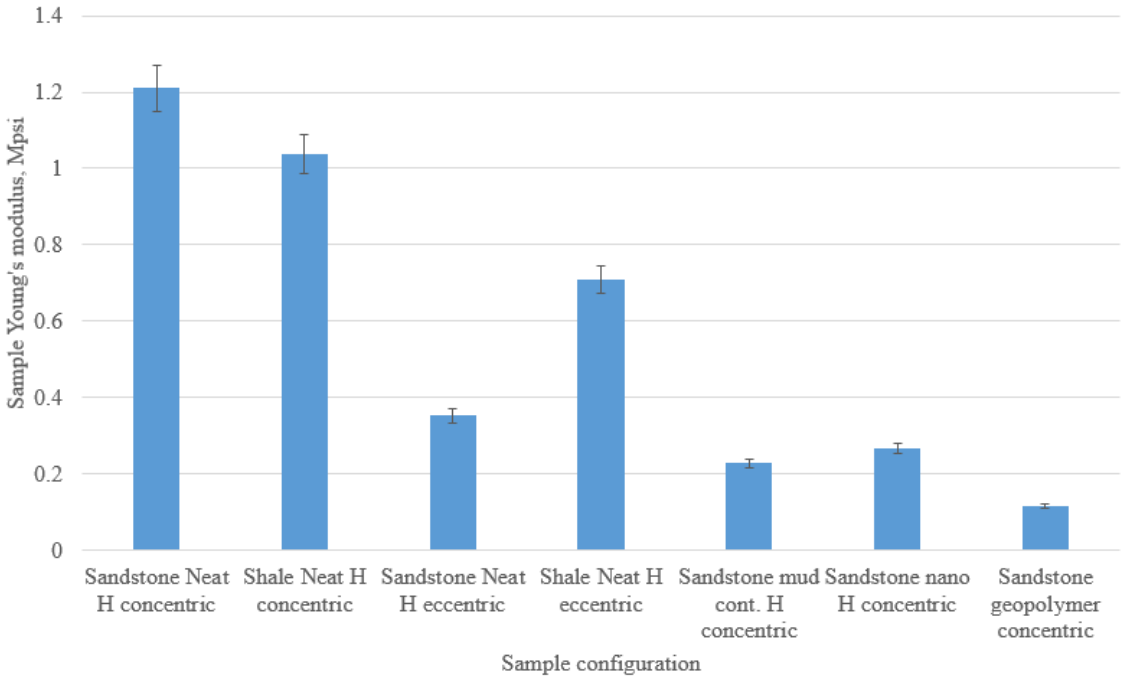

Figure 52 – Sample Young's modulus for each sample configuration

Compared to the base Neat Class H in sandstone with concentric pipe, the shale system with concentric pipe had a 14% lower Young's modulus. Due to eccentricity and mud-contamination, the sandstone-Neat Class H system recorded a 71% and 81% lower Young's modulus respectively. For the shale systems, the Young's modulus dropped by 32% due to eccentricity of the pipe. Since mud contamination and eccentricity are detrimental to the well integrity, these values of Young's modulus are a representation of the degree of effect to the process of bond integrity.

It is recommended that the cement that is used as a barrier in the oil well should have a low Young's modulus and a high Poisson's ratio. This would mean that the cement is ductile and deforms substantially during casing loading but the bond integrity is still intact during the deformation of the casing. The addition of nano-synthetic graphite reduced the sample Young's modulus by 77%

while geopolymer system had 90% less Young's modulus. This is advantageous to the fact that these cement systems require a higher load to cause cement and bond failure.

5. Conclusions

This research introduces a novel paradigm in the experimental investigation of the bonding of oil well cements to both subsurface formations and the casing. The combination of microscope imaging and digital image correlation (DIC) provided insight into the bonding dynamics of cement with the annular substrate surfaces. Under the aforementioned experimental conditions and based on the results obtained, these are the conclusions:

- The microscope imaging provided insight to the formulation of the cement bond with sandstone, shale and steel. The images showed the mechanical interlocking bond formed at the Neat Class H-sandstone interface and revealed the continuous bond interface between Neat Class H and shale due to much smaller grain size.
- Because of these lithological aspects, DIC revealed that there was strain generated at the cement-shale interface while there is no strain along the cement-sandstone interface during loading of the Neat H cement system. Results showed that it required 20% less maximum load to cause the sample failure in the shale-Neat Class H-concentric system compared to the sandstone system.
- Even with a 28% higher deformation, the load required to cause failure of the interfacial bond between Class H cement contaminated by 10% water-based mud and steel is 76% less than that of Neat Class H cement.
- The steel ‘casing’ eccentricity (50%) had similar detrimental effect to the cement bond integrity as mud-contaminated cement as it requires 60% less load before the sandstone sample system failed. Results also showed that it required 38% less load to cause failure in the Neat H in shale samples due to the same eccentricity.

- Unconfined compressive strength tests after 24 hours of cement (70^{o}C temperature) curing showed 38% lower UCS in the nano-modified (0.5% BWOC) Class H system than Neat Class H. The geopolymer cement had 63% lower UCS. This influenced the deformation characteristics of the samples.
- Even with 63% less maximum failure load, geopolymer cement system incurred 54% higher deformation before failure compared to the Neat H sample system. The sample system also had a 90% lower Young's modulus.
- With 38% less maximum failure load, the addition of nano-synthetic graphite resulted in 140% higher system deformation before sample failure. The sample system recorded a 77% lower Young's modulus compared to the Neat Class H sample system.

6. Recommendations

Digital Image correlation technique applied under Indirect tensile stress conditions is a method of studying bonding dynamics but there are limitations to the study that produced the results stated above. These are recommendations on further research:

- For oil-field cementing operations, nano-synthetic graphite should be integrated into the design of cementing operations because of the higher mechanical and better bonding characteristics.
- Geopolymer cements should be field-tested in order to verify their viability as potential replacements to Ordinary Portland cement with the available research on both mechanical and bonding properties.
- The loading scheme for this research was from the formation side. The effect of internal casing loading should be investigated to thoroughly represent the generic wellbore under stress.
- The cement samples were cured under water for 24 hours before testing was carried out. The effect of curing time on the bonding dynamics should be investigated with different cement systems to provide a clearer understanding of the strength of both the cement and its bond.
- The cement samples were cured at an elevated temperature of 70^{o}C (158^{o}F). The effect of curing temperature should also be investigated to cater for varying subsurface temperature conditions.
- The effect of pipe roughness should also be investigated because to also define the strain deformation of different roughness of pipes combined with other system conditions.

- The loading rate used was 0.1mm/min which was limited by the number of frames that could be taken by the camera software. A lower loading rate should be applied to have more detail about strain deformation if the limitation of the DIC software is fixed.
- The application of confining pressure should be investigated to portray a generic subsurface wellbore condition.
- Mathematical and numerical simulation should be carried out to depict the strain deformation behavior of these samples under these conditions. This will hopefully be extended into research for mechanical characteristics of desired cement systems under particular subsurface conditions.

References

Ahmed, S., Ezeakacha, C.P. and Salehi, S. 2018. Improvement in Cement Sealing Properties and Integrity Using Conductive Carbon Nano Materials: From Strength to Thickening Time. Paper presented at the SPE Annual Technical Conference and Exhibition, Dallas, Texas, U.S.A., 24-26 September. SPE-191709-MS. http://dx.doi.org/10.2118/191709-MS.

Ahmed, S., Salehi S., Ezeakacha, C. P. and Teodoriu, C. 2019a. Experimental Investigation of Elastomers in Downhole Seal Assembly: Implications for Safety. *Journal of Polymer Testing* **76**: 350-364. https://doi.org/10.1016/j.polymertesting.2019.03.041.

Ahmed, S., Salehi S., Ezeakacha, C. P. and Teodoriu, C. 2019b. Evaluation of Liner Hanger Seal Assembly and Cement Sheath as a Dual Barrier System: Implications for Industry Standards. *Journal of Petroleum Science and Engineering* **178**: 1092-1103. https://doi.org/10.1016/j.petrol.2019.04.017.

Al Ramadan, M., Salehi, S., Kwatia, G. et al. 2019. Experimental Investigation of Well Integrity: Annular Gas Migration in Cement Column. *Journal of Petroleum Science and Engineering.* https://doi.org/10.1016/j.petrol.2019.04.023.

Amani, M., Al-Jubouri, M. and Shradavan, A. 2012. Comparative Study of Using Oil-Based Mud Versus Water-Based Mud in HPHT Fields. *Advances in Petroleum Exploration and Development* **4**(2): 18-27. http://dx.doi.org/10.3968/j.aped.1925543820120402.987.

American Petroleum Institute. 2010. ANSI/API Spec 10A – Specification for Cements and Materials for Well Cementing. Washington, D.C.: American Petroleum Institute.

American Petroleum Institute. 2013. API RP 10B-2 – Recommended Practice for Testing Well Cements. Washington, D.C.: American Petroleum Institute.

Andrade, J. De., Torsaeter, M. and Todorovic, J. 2014. Influence of casing centralization on cement sheath integrity during thermal cycling. Paper presented at the IADC/SPE Drilling Conference and Exhibition, Fort Worth, Texas, U.S.A., 4-6 March. SPE-168012-MS. https://doi.org/10.2118/168012-MS.

Asbury Carbons. 2018. http://asburystore.com/Articles.asp?ID=250.

ASTM International, 2016. ASTM D3967-16 Standard Test Method for Splitting Tensile Strength of Intact Rock Core Specimens. https://doi.org/10.1520/D3967-16.

Aïtcin, P, and Flatt, R.J. 2016. *Science and Technology of Concrete Admixtures.* Elsevier.

Barton, C.C. 1982. Variables In fracture Energy and Toughness Testing of Rock. Paper presented at the 23rd U.S. Symposium on Rock Mechanics (USRMS), Berkeley, California, U.S.A., 25-27 August. ARMA-82-449.

Bwala, A.H. 2015. *Experimental Investigation of Shear Bond Strength and Microstructure of Fly Ash Geopolymer Cement for Oil and Gas Industry*. MS Thesis, University of Louisiana at Lafayette, Lafayette, Louisiana (May 2015).

Bosma, M., Ravi, K., van Driel, W. et al. 1999. Design Approach to Sealant Selection for the Life of the Well. Paper presented at the Annual Technical Conference and Exhibition, Houston, Texas, U.S.A., 3 – 6 October. SPE-56536-MS. https://doi.org/10.2118/56536-MS.

Bourgoyne Jr., A.T., Chenevert, M.E., Millheim, K.K. et al. 1991. Applied Drilling Engineering, Vol. 2. Richardson, Texas: Textbook Series, SPE.

BP Energy Outlook. 2017. https://www.bp.com/content/dam/bp/pdf/energy-economics/energy-outlook-2017/bp-energy-outlook-2017.pdf.

Bybee, K. 2002. High-Pressure/High Temperature Cementing. Journal of Petroleum Technology, 54(8): 58-61. https://doi.org/10.2118/0802-0058-JPT.

Bybee, K. 2004. Analysis of Tensile-Strength Test Methods for Oilfield cement. *Journal of Petroleum Technology* 56(08): 62 – 64. https://doi.org/10.2118/0804-0062-JPT.

Correlated Solutions, 2009. Vic-2D Testing Guide. http://www.correlatedsolutions.com/supportcontent/Vic-2D-v6-Testing-Guide.pdf.

Couturier, M., Guillot, D., Henriks, H. et al. 1990. Design Rules and Associated Spacer properties for Optimal Mud removal in Eccentric Annuli. Paper presented at the Petroleum Society of Canada Annual Technical Meeting, Calgary, Alberta, Canada, 10-13 June. PETSOC-90-112. https://doi.org/10.2118/90-112.

Chu, T.P., Sutton, M. and Ranson, W.F. Application of of digital-image correlation techniques to experimental mechanics. *Experimental Mechanics* **25**(3): 232-244. https://10.1007/BF02325092.

Churcher, P.L., French, P.R., Shaw, J.C. et al. 1991. Rock Properties of Berea Sandstone, Baker Dolomite and Indiana Limestone. Paper presented at the SPE International Symposium on Oilfield Chemistry, Anaheim, California, U.S.A., 20-22 February. SPE-21044-MS. https://doi.org/10.2118/21044-MS.

Davidovits, J. 1999. Chemistry of Geopolymeric Systems, Terminology. Proceedings of the 2nd International Conference, Géopolymère, pp. 9–39, Saint-Quentin, France.

Davidovits, J. 2011. Geopolymer Chemistry and Applications. Third ed. Institut Geopolymere, Saint-Quentin, France. ISBN: 9782951482050.

Dawson, G.K.W., Pearce, J.K., Biddle, D. et al. 2014. Experimental mineral dissolution in BereaSandstone reacted with CO_2 or SO_2-CO_2 in NaCl brine under CO_2 sequestration conditions. *Chemical Geology* **399**: 87-97. https://doi.org/10.1016/j.chemgeo.2014.10.005.

Dusseault, M.B., Gray, M.N. and Nawrocki, P.A. 2000. Why Oilwells Leak: Cement Behavior and Long-term Consequences. Paper presented at the International Oil and Gas Conference and Exhibition, Beijing, China, 7 – 10 November. SPE-64733-MS. https://doi.org/10.2118/64733-MS.

Duxson, P., Fernandez-Jimenez, A., Provis, J. et al. 2007. Geopolymer Technology. The Current State of The Art. Journal of Materials Science 42(9): 2917-2933. https://doi.org/10.1007/s10853-006-0637-z.

Saleh, F.K., Salehi, S. and Teodoriu, C. 2019. Experimental Investigation of mixing energy of well cements: The gap between laboratory and field mixing. *Journal of Natural Gas Science and Engineering* **63**: 47-57. https://doi-org.ezproxy.lib.ou.edu/10.1016/j.jngse.2019.01.004.

Ferda, A. and Al-Ghadban, H.H. 2004. Simulation Investigation of Casing Eccentricity Estimation for Different Inclination Angles and Tensile Forces using Finite Element Method. Paper presented at the SPE International Petroleum Conference, Puebla Pue., Mexico, 7-9 November. SPE-91811-MS. https://doi.org/10.2118/91811-MS.

Fink, J. 2015. Petroleum Engineer's Guide to Oil Field Chemicals and Fluids. 2nd Ed. Elsevier.

Gasda, S. E., Bachu, S. and Celia, M. A. 2004. Spatial characterization of the location of potentially leaky wells penetrating a deep saline aquifer in a mature sedimentary basin. Environmental Geology 46(6-7): 707-720. https://doi.org/10.1007/s00254-004-1073-5.

Garnier, A., Fraboulet, B., Saint-Marc, J. et al. 2007. Characterization of Cement systems to ensure Cement Sheath Integrity. Paper presented at the Offshore Technology Conference, Houston, Texas, U.S.A., 30 April – 3 May. OTC-18754-MS. https://doi.org/10.4043/18754-MS.

Ghouri, S. 2008. Global LNG Outlook- Challenges and Opportunities. Paper presented at the 19th World Petroleum Congress, Madrid, Spain, 29 June – 3 July. WPC-19-1280.

Guohua, W., Zhengmao, C., Jiyou, X. et al. 2012. Study on the Effect of Non-Uniformity Load and Casing Eccentricity on the Casing Strength. *Energy Procedia* **14**: 285-291. https://doi.org/10.1016/j.egypro.2011.12.931.

Hibbert, A.P., Kellingray, D.J. and Vidick, B. 1995. Effect of mixing energy levels during batch mixing of cement slurries. *SPE Drilling and Completions* **10**(1): 49-52. https://doi.org/10.2118/25147-PA.

Ichim, A. 2015. Effect of Cement Thermal Properties on Heat Transfer in HP/HT Wells.

Ichim, A. 2017. *Experimental Determination of Oilfield Cement Properties and their Influence on Well Integrity.* MS thesis, University of Oklahoma, Norman, Oklahoma (May 2017).

Jafariesfad, N., Geiker, M.R., Gong, Y. et al. 2017. Cement sheath modification using nanomaterials for long-term zonal isolation of oil wells: Review. *Journal of Petroleum Science and Engineering* **156**: 662-672. https://doi.org/10.1016/j.petrol.2017.06.047.

Kauffman, E.G., Berggren, W. and Van Couvering, J. 1984. Catastrophes and Earth History: The New Uniformitarianism. edited by W. A. Berggren and J. A. Van Couvering, pp. 151–246, Princeton Univ. Press, Princeton, N. J. https://www.jstor.org/stable/j.ctt7zv4gv.

Khalifeh, M., Saasen, A., Vrålstad, T. et al. 2015. Experimental study on the synthesis and characterization of aplite rock-based geopolymers. *Journal of Sustainable Cement-Based Materials* **5**(4): 233-246. http://dx.doi.org/10.1080/21650373.2015.1044049.

Khalifeh, M., Todorovic, J., Vralstad, T. et al. 2016. Long-term durability of rock-based geopolymers aged at downhole conditions for oil well cementing operations. *Journal of Sustainable Cement-Based Materials* **6**(4): 217-230. https://doi.org/10.1080/21650373.2016.1196466.

Khalifeh, M., Saasen, A., Hodne, H. et al. 2017a. Geopolymers as an Alternative for Oil Well Cementing Applications: A review of Advantages and Concerns. Paper presented at the ASME 36th International Conference on Ocean, Offshore and Arctic Engineering, Trondheim, Norway, 25-30 June. https://doi.org/10.1115/OMAE2017-61227.

Khalifeh, M., Saasen, A., Larsen, H.B., and Hodne, H. 2017b. Development and characterization of norite-based cementitious binder from an ilmenite mine waste stream. *Journal of Advances in Materials Science and Engineering* **2017**. https://dx.doi.org/10.1155/2017/6849139.

Khalifeh, M., Saasen, A., Hodne, H. et al. 2018. Laboratory Evaluation of Rock-based Geopolymers for Zonal Isolation and Permanent P&A Applications. *Journal of Petroleum Science and Engineering* **175**: 352-362. https://doi.org/10.1016/j.petrol.2018.12.065.

Kimanzi, R.J., Harshkumar, P., Salehi, S., Teodoriu, C. and Khalifeh, M. 2019. Potentials of Nano-designed plugs: Implications for short and long term well integrity. 38th International Conference on Ocean, Offshore and Arctic Engineering, 9-14 June, 2019.

Kiran, R., Teodoriu, C., Dadmohammadi, Y. et al. 2017. Identification and evaluation of well integrity and causes of failure of well integrity barriers (A review). Journal of Natural Gas Science and Engineering 45: 511-526. https://doi.org/10.1016/j.jngse.2017.05.009.

LabWrench. 2017. Instron 5980 specifications. http://www.labwrench.com/?equipment.view/equipmentNo/24619/Instron/5980.

Li, Z. and Schieber, J. 2018. Composite Particles in Mudstones: Examples from the Late Cretaceous Shale Member of the Mancos Shale Formation. *Journal of Sedimentary Research* **88**: 1319-1344. https://dx.doi.org/10.2110/jsr.2018.69.

Loizzo, M., Lecampion, B. and Mogilevskaya, S. 2017. The role of geological barriers in achieving robust well integrity. Energy Procedia 114: 5193-5205. https://doi.org/10.1016/j.egypro.2017.03.1673.

Ma, Y., Cui, M., Guo, X. et al. 2007. How to evaluate the Effect of Mud cake on Cement Bond Quality of Second Interface. Paper presented at the SPE/IADC Middle East Drilling Technology Conference and Exhibition, Cairo, Egypt, 22 – 24 October. SPE-108240-MS. https://doi.org/10.2118/108240-MS.

Matsuzawa, M., Umeza, S. and Yamamoto, K. 2006. Evaluation of Experiment Program 2004: Natural Hydrate Exploration Campaign in the Nankai-trough Offshore Japan. Paper presented at

the IADC/SPE Drilling Conference, Miami, Florida, U.S.A., 21-23 February. SPE-98960-MS. https://doi.org/10.2118/98960-MS.

Mokhtari, M., Hayatdavoudi, A., Nizamutdinov, R. et al. 2017. Characterization of complex fracture propagation in naturally fractured formations using Digital Image Correlation technique. Paper presented at the SPE Hydraulic Fracturing Technology Conference and Exhibition, The Woodlands, Texas, U.S.A., 24-26 January. SPE-184826-MS. https://doi.org/10.2118/184826-MS.

Nath, F., Salvati, P.E., Mokhtari, M. et al. 2017. Observation of Fracture Growth in Laminated Sandstone and Carbonate Samples under Brazilian Testing Conditions Using Digital Image Correlation Technique. Paper presented at te SPE Eastern Regional Meeting, Lexington, Kentucky, U.S.A., 4-6 October. SPE-187515-MS. https://doi.org/10.2118/187515-MS.

Nath, F., Kimanzi, R.J., Mokhtari, M. et al. 2018. A novel method to investigate cement-casing bonding using digital image correlation. *Journal of Petroleum Science and Engineering* **166**: 482-489. https://doi.org/10.1016/j.petrol.2018.03.068.

Nygaard, R., Salehi, S., Weideman, B. et al. 2014. Effect of Dynamic Loading on Wellbore Leakage for the Wabamun Area CO2-Sequestration project. Journal of Canadian Petroleum Technology 53(1): 69-82. https://doi.org/10.2118/146640-PA.

NORSOK. Regulation D-010. 2004a. Well integrity in drilling and well operations. 3rd revision 2004-08.

Paiva, M.D.M., Silva, E.C.C.M., Melo, D.M.A. et al. 2018. A Geopolymer cementing system for oil wells subject to steam injection. *Journal of Petroleum Science and Engineering* **169**: 748-759. https://doi.org/10.1016/j.petrol.2018.06.022.

Pan, B., Qian, K.M., Xie, H.M., and Asundi, A., 2009. Two-dimensional digital image correlation for in-plane displacement and strain measurement: a review. *Measurement Science Technology* **20(**6). http://dx.doi.org/10.1088/0957-0233/20/6/062001.

Patel, H. and Salehi, S. 2019a. Development of Advanced Finite Element Model and Parametric Study to Evaluate Cement Sheath Barrier. *Journal of Energy Resources Technology* **141**(9). http://dx.doi.org/10.1115/1.4043137.

Patel, H. and Salehi, S. 2019b. Investigation of Elastomer Seal Energization: Implications for Conventional and Expandable Hanger Assembly. *Energies* **12**(4). https://doi.org/10.3390/en12040763.

Patel, H., Salehi, S., Teodoriu, C. et al. R. 2019c. Performance evaluation and parametric study of elastomer seal in conventional hanger assembly. *Journal of Petroleum Science and Engineering* **175**: 246–254. http://dx.doi.org/10.1016/j.petrol.2018.12.051.

Patil, R. and Deshpande, A. 2012. Use of Nanomaterials in cementing applications. Paper presented at the SPE International Oilfield Nanotechnology Conference, Noordwijk, The Netherlands, 12-14 June. SPE-155607-MS. http://dx.doi.org/10.2118/155607-MS.

Peterson, B. 1963. Bond of cement compositions for cementing wells. Paper presented at the 6th World Petroleum Congress, Frankfurt am Main, Germany, 19-26 June. WPC-10123.

Peyvandi, A., Taleghani, A. D., Soroushian, P. and Cammarata, R. 2017. The Use of Low-Cost Graphite Nanomaterials to Enhance Zonal Isolation in Oil and Gas Wells. Paper presented at the SPE Annual Technical Conference and Exhibition, San Antonio, Texas, U.S.A., 9–11 October. SPE-187105-MS. http://dx.doi.org/10.2118/187105-MS.

Rangan, B.V. 2014. Geopolymer concrete for environmental protection. *The Indian Concrete Journal* **88**(4): 41-59. http://hdl.handle.net/20.500.11937/29749.

Ryan, D.F., Kellingray, D.S. and Lockyear, C.F. 1992. Improved Cement Placement on North Sea Wells using a Cement Placement Simulator. Paper presented at the European Petroleum Conference, Cannes, France, 16 -18 November. SPE-24977-MS. https://doi.org/10.2118/24977-MS.

Saleh, F.K., Rivera, R., Salehi, S. et al. 2018. How Does Mixing Water Quality Affect Cement Properties. Paper presented at the SPE International Conference and Exhibition on Formation Damage Control, Lafayette, Louisiana, U.S.A., 7-9 February. SPE-189505-MS. https://doi.org/10.2118/189505-MS.

Salehabadi, M., Yang, J., Ahmed, R. et al. 2010. Effect of Casing Eccentricity on Casing Stability Analysis in wellbores drilled in Gas Hydrate Bearing Sediments. Paper presented at the SPE EUROPE/EAGE Annual Conference and Exhibition, Barcelona, Spain, 14-17 June. SPE-131236-MS. https://doi.org/10.2118/131236-MS.

Salehi, S., Khattak, M.J. and Rizvi, H. R. 2016a. Development of Geopolymer-based Cement slurries with enhanced thickening time, compressive and shear bond strength and durability. Paper presented at the IADC/SPE Drilling Conference and Exhibition, Fort Worth, Texas, U.S.A., 1 – 3 March. SPE-178793-MS. https://doi.org/10.2118/178793-MS.

Salehi, S., Ali, N. and Khattak, M.J. 2016b. Geopolymer Composites as Efficient and Economical Plugging Materials in Peanuts Price Oil Market. Papers presented at the SPE Annual Technical Conference and Exhibition, Dubai, U.A.E., 26-28 September. SPE-181426-MS. https://doi.org/10.2118/181426-MS.

Salehi, S., Khattak, M.J., Bwala, A.H. et al. 2017. Characterization, morphology and shear bond strength analysis of geopolymers: Implications for oil and gas well cementing applications. *Journal of Natural Gas Science and Engineering* **38**: 323-332. http://dx.doi.org/10.1016/j.jngse.2016.12.042.

Scott, J. B. and Brace, R. L. 1966. Coated casing- "A technique for improved cement bonding". Paper presented at the Drilling and Production Practice, New York, New York, U.S.A., 1 January. API-66-043.

Shale Experts. 2016. Tuscaloosa Marine Shale (TMS) Overview. https://www.shaleexperts.com/plays/tuscaloosa-marine-shale/Overview.

Sutton, M.A., McNeill, S.R., Helm, J.D. et al. 2000. Advances in two-dimensional and three-dimensional computer vision. *Photo-mechanics Topics Applied Physics* **77**: 323-372. https://doi.org/10.1007/3-540-48800-6_10.

Sutton, M.A., Orteu. J.J., and Schreier, H.W. 2009. Image Correlation for Shape, Motion and Deformation Measurements. Springer publishers.

Teodoriu, C., Yi, M.C., Ichim, A. et al. 2018. A Novel View of Cement Failure with Application to Geothermal Well Construction. *43rd Workshop on Geothermal Reservoir Engineering, Stanford University*: 12-14. SGP-TR-213.

Thiercelin, M.J., Dargaud, B., Baret, J.F. et al. 1998. Cement design based in Cement mechanical response. Society of Petroleum Engineers 13(4): 266-273. https://doi.org/10.2118/52890-PA.

Vrålstad, T., Todorovic, J, Saasen, A. et al. 2016. Long-Term Integrity of Well Cements at Downhole Conditions. Paper presented at the SPE Bergen One Day Seminar, Bergen, Norway, 20 April. SPE-180058-MS. https://doi.org/10.2118/180058-MS.

Vrålstad, T., Saasen, A., Fjær, E. et al. 2018. Plug & abandonment of offshore wells: Ensuring long-term well integrity and cost-efficiency. *Journal of Petroleum Science and Engineering* **173**: 478-491. https://doi.org/10.1016/j.petrol.2018.10.049.

Williams, R.H., Khatri, D.K., Roy-Delage, S.L. et al. 2011. Flexible, Expanding Cement System (FECS) successfully provides Zonal Isolation across Marcellus Shale Gas Trends. Paper presented at the Canadian Unconventional Resources Conference, Calgary, Alberta, Canada, 15-17 November. SPE-149440-MS. https://doi.org/10.2118/149440-MS.

Wilson D.C., Eustes, A.W. and Fleckenstein, W.W. 2018. Lab Testing Cement-Steel Bonding at Shallow Temperature and Pressure Conditions. Paper presented at the SPE Western Regional Meeting, Garden Grove, California, U.S.A., 22 – 26 April. SPE-190031-MS. https://doi.org/10.2118/190031-MS.

Xie, L., Chaudhary, S. and Chen, Z. 2015. Analysis of the Effect of Eccentricity on Displacement of Non-Newtonian fluids with a Hybrid method. Paper presented at the SPE Annual Technical Conference and Exhibition, Houston, Texas, U.S.A., 28-30 September. SPE-174909-MS. https://doi.org/10.2118/174909-MS.

Yu, Y., Zhang, J., and Zhang, J. 2009. A modified Brazilian disk tension test. *International Journal of Rock Mechanics and Mining Sciences* **46**(2): 421-425. https://doi.org/10.1016/j.ijrmms.2008.04.008.

Zhang, H., Huang, G., Song, H. et al. 2012. Experimental investigation of deformation and failure mechanisms in rock under indentation by digital image correlation. *Engineering Fracture Mechanics* **96**: 667-675. https://doi.org/10.1016/j.engfracmech.2012.09.012.

Zhang, S. and Sheng, J.J. 2018. Effect of Water Imbibition on Fracture Generation in Mancos Shale under Isotropic and Anisotropic Stress Conditions. *Journal of Geotechnical and Geoenvironmental Engineering* **144**(2): https://doi.org/10.1061/(ASCE)GT.1943-5606.0001832.

Appendix A: Principles of Digital Image Correlation (DIC)

The concept of image matching is not a recent concept. Image matching is applied in license plate recognition, process control, geological mapping and has been extended to concepts in space exploration (Sutton et al. 2009). Digital image correlation utilizes special algorithms to study surface strain deformation and the physics behind that. There is still the concern for resolution which are very specific in the engineering applications. For this research, digital images of the specimen were collected at fixed or variable time intervals (Nath et al. 2017). The first image was the undeformed painted specimen with distributed image pixels. The digital image correlation processes the distribution and displacement of the image pixels (Correlated Solutions, 2009).

The strain deformation on the images is evaluated by creating a time-dependent step-by-step analysis of the different images. The pixelation for the images is software-dependent and is chosen by the user of the software. Since the recommended painting scale is white and black, a variation in grey levels is the underlying principle for image analysis. This gives the software the ability to distinctively measure the distortion in the images taken. A region of interest (ROI) must be verified during the DIC image processing of the surface. This specific region is demarcated into evenly spaced virtual grids and the pixel displacements are evaluated within each grid to compute the full-field deformation as shown in **Figure A1**.

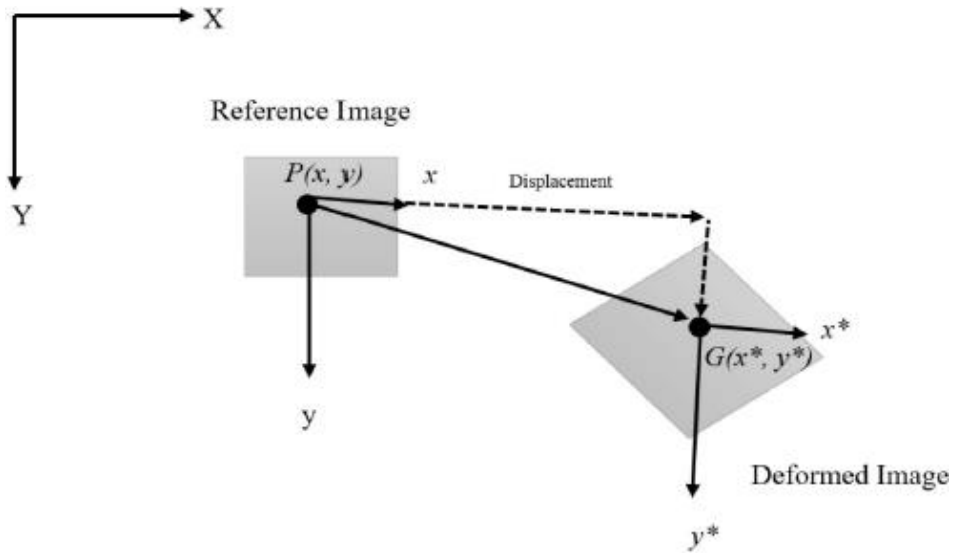

Figure A1 - DIC visual analysis principle (Nath et al. 2017)

Point P(x,y) represents the pixel as its center and its image is tracked to the point after displacement. The resultant position is also recorded and using correlation criterion, the strain as a function of displacement is calculated and matched in response. The initial and resultant (deformed) points of reference are matched for similarity before any correlation occurs. This process is carried out along the entire region of interest to attain progression of deformation. The pixel resolution is critical but it is recommended to have smaller grids to increase the spatial resolution (Nath et al. 2017) but this is subject to computational power. The displacement within the ROI can be computed using the correlation coefficient (Zhang et al. 2012) **Equation A-1**:

$$C(X) = \frac{\sum_{i=1}^{m}\sum_{j=1}^{m}[f(x_i,y_j)-\overline{f}].\left[f\left(x_i^*,y_j^*\right)-\overline{g}\right]}{\sqrt{\sum_{i=1}^{m}\sum_{j=1}^{m}[f(x_i,y_j)-\overline{f}]^2.\sum_{i=1}^{m}\sum_{j=1}^{m}[f\left(x_i^*,y_j^*\right)-\overline{g}]^2}} \quad \text{.....A-1}$$

Where:

$$x^* = x + u + \frac{\partial u}{\partial x}\Delta x + \frac{\partial u}{\partial y}\,\Delta y$$

$$y^* = y + v + \frac{\partial v}{\partial x}\Delta x + \frac{\partial v}{\partial y}\,\Delta y$$

$$X = (u, v, \frac{\partial u}{\partial x}, \frac{\partial u}{\partial y}, \frac{\partial v}{\partial x}, \frac{\partial v}{\partial y})$$

Horizontal displacement field, *u = u(x,y),*

Vertical displacement field, *v = v(x,y)*

Gray level value at (x,y) at initial/reference image, f = f(x,y)

Gray level at coordinate (x*,y*) at time step image, g = g(x*,y*)

$\bar{f}$ and $\bar{g}$ are mean values of the two gray level values

Pan et al. (2009) formulated an explicit numerical equation for the strain tensor shown as **Equation A-2** while the axial strain can be calculated using **Equation A-3** by Sutton et al. (2009):

$$\varepsilon = \begin{bmatrix} \frac{\partial u}{\partial x} & \frac{1}{2}(\frac{\partial u}{\partial y} + \frac{\partial v}{\partial x}) \\ \frac{1}{2}(\frac{\partial u}{\partial y} + \frac{\partial v}{\partial x}) & \frac{\partial v}{\partial y} \end{bmatrix} \quad \text{……A-2}$$

$$\varepsilon_{xx} = \frac{\partial u}{\partial x} + \frac{1}{2}[\,(\frac{\partial u}{\partial x})^2 + (\frac{\partial v}{\partial x})^2] \quad \text{……A-3}$$

Appendix B: Microscope images

The available Keyence laser microscope takes images under different magifications: 5x, 10x, 20x 100x and 200x. 20x was used for this research because it has the capability to clerly show the bonding interface between the cement and the steel pipe or sandstone/shale. This appendix will be a display of the various microscope images taken of different points of the interfaces for different samples.

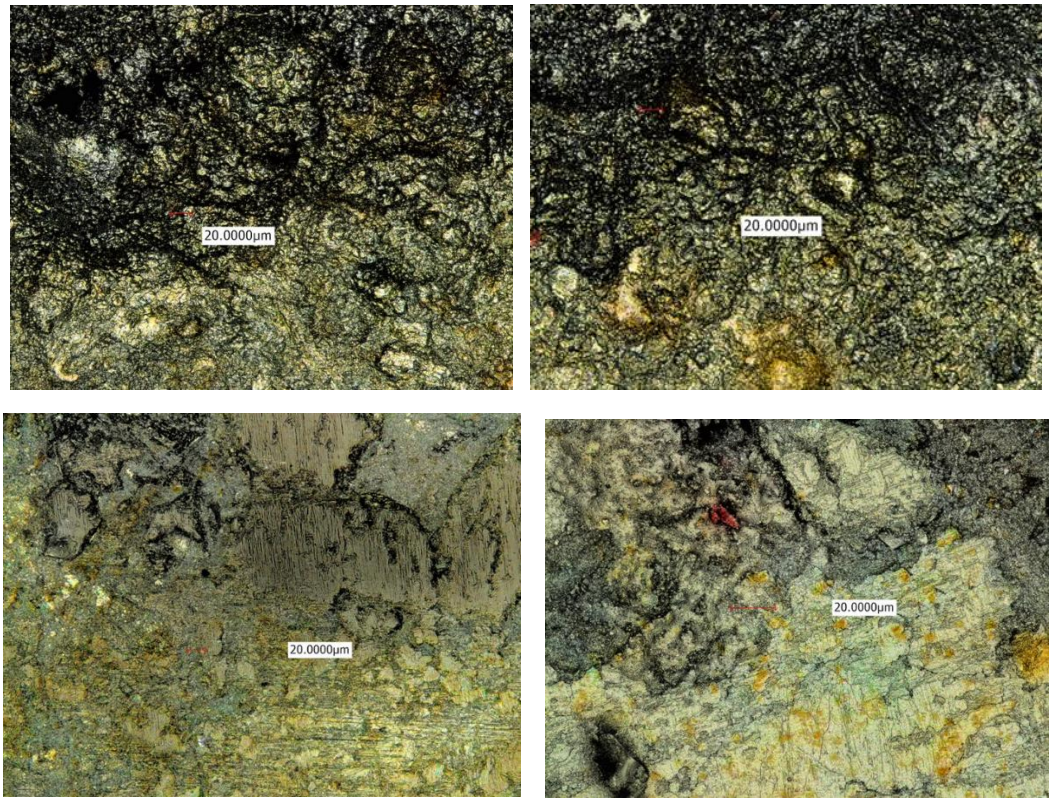

Figure B1 – Microscope images at different points of the interface between Neat Class H cement (bottom layer) and sandstone (top layer)

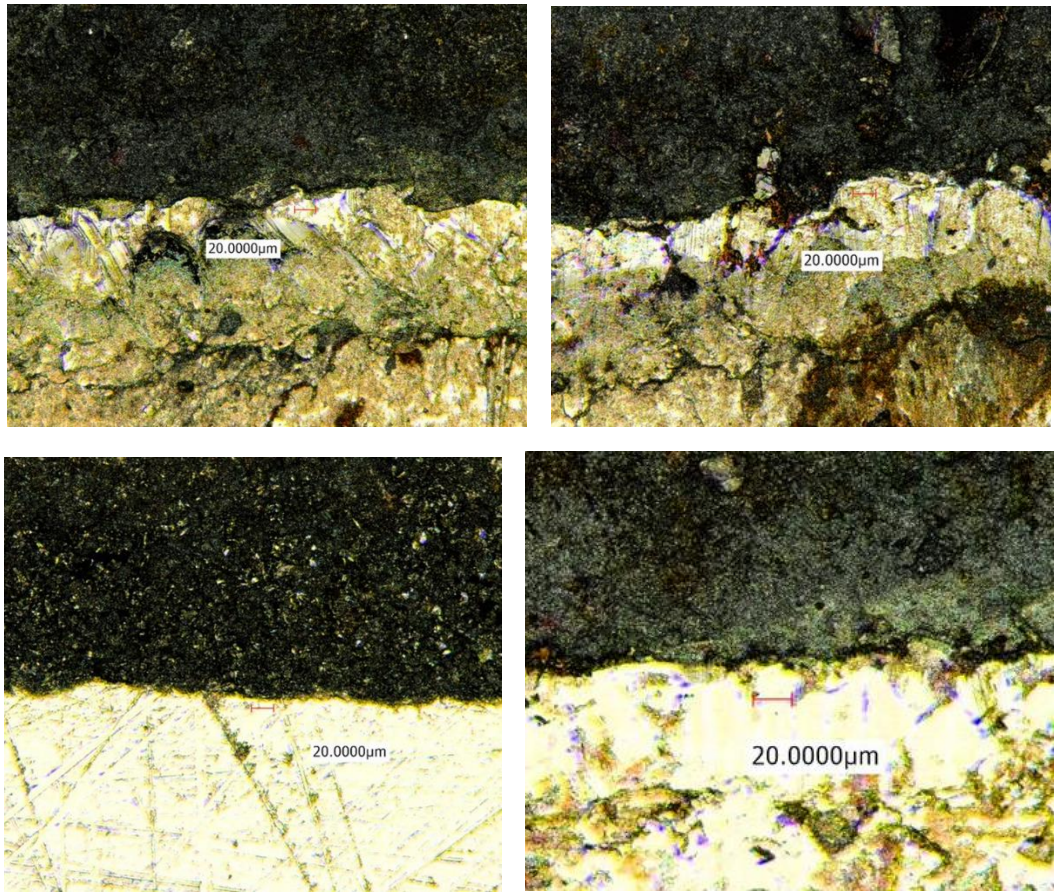

Figure B2 – Microscope images at different points of the interface between Neat Class H cement (top layer) and steel (top layer)

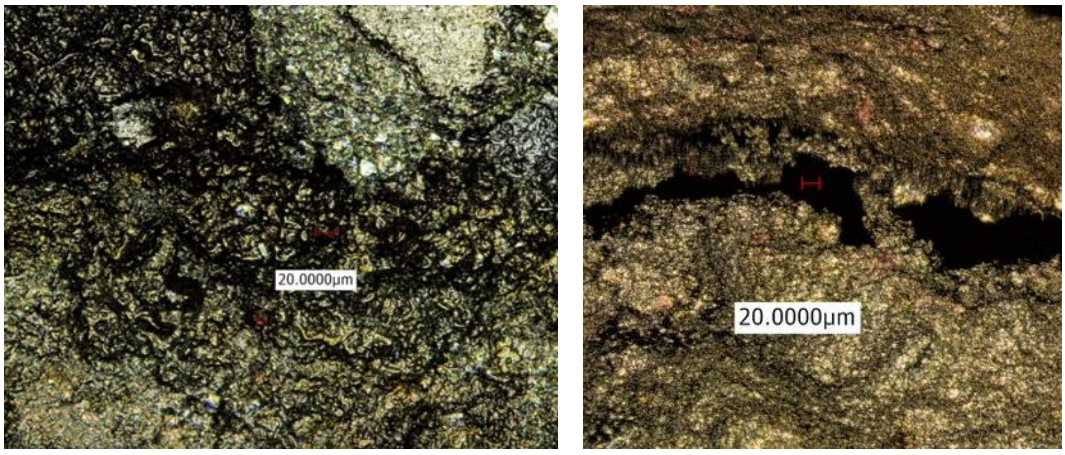

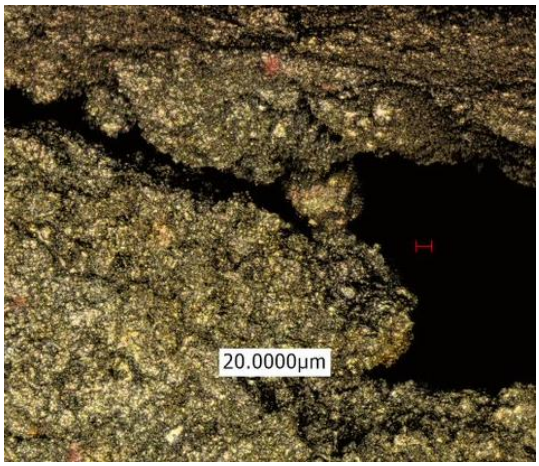

Figure B3 – Microscope images at different points of the interface between mu-contaminated H cement (bottom layer) and sandstone (top layer)

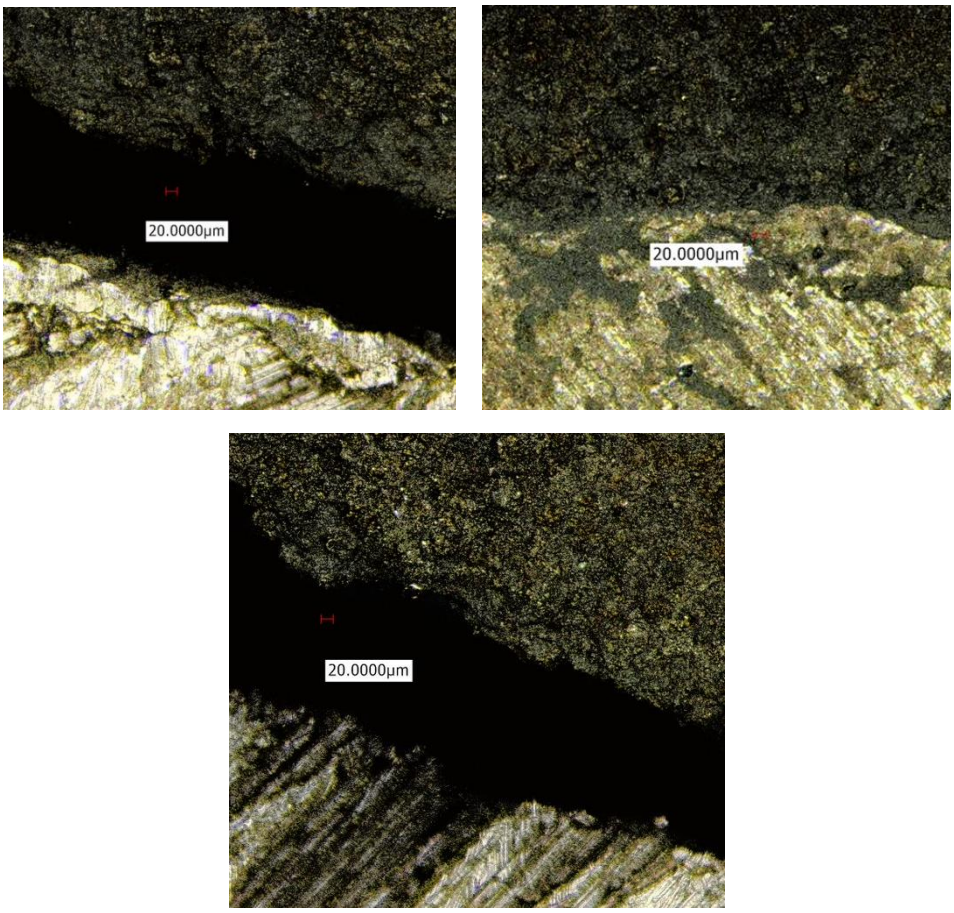

Figure B4 – Microscope images at different points of the interface between mu-contaminated H cement (top layer) and steel (bottom layer)

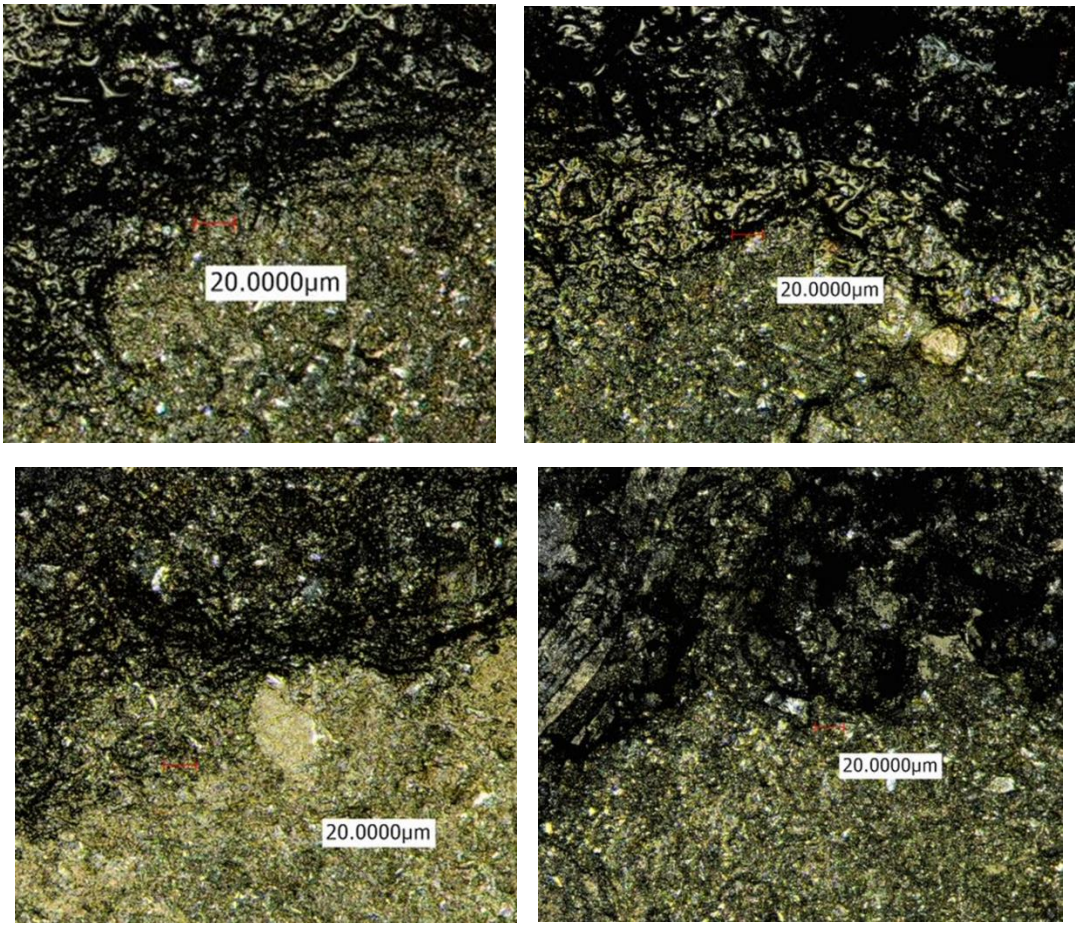

Figure B5 – Microscope images at different points of the interface between Nano-modified H cement (bottom layer) and sandstone (top layer)

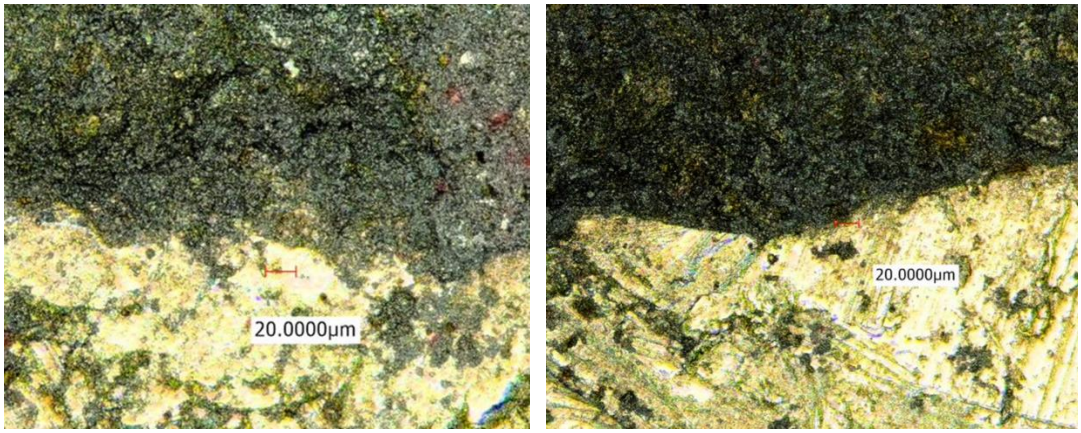

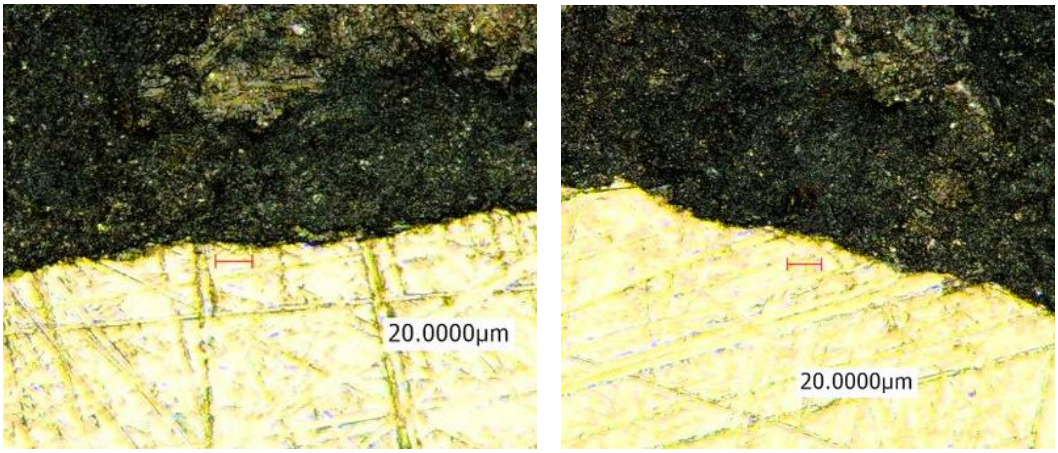

Figure B6 – Microscope images at different points of the interface between Nano-modified H cement (top layer) and steel (bottom layer)

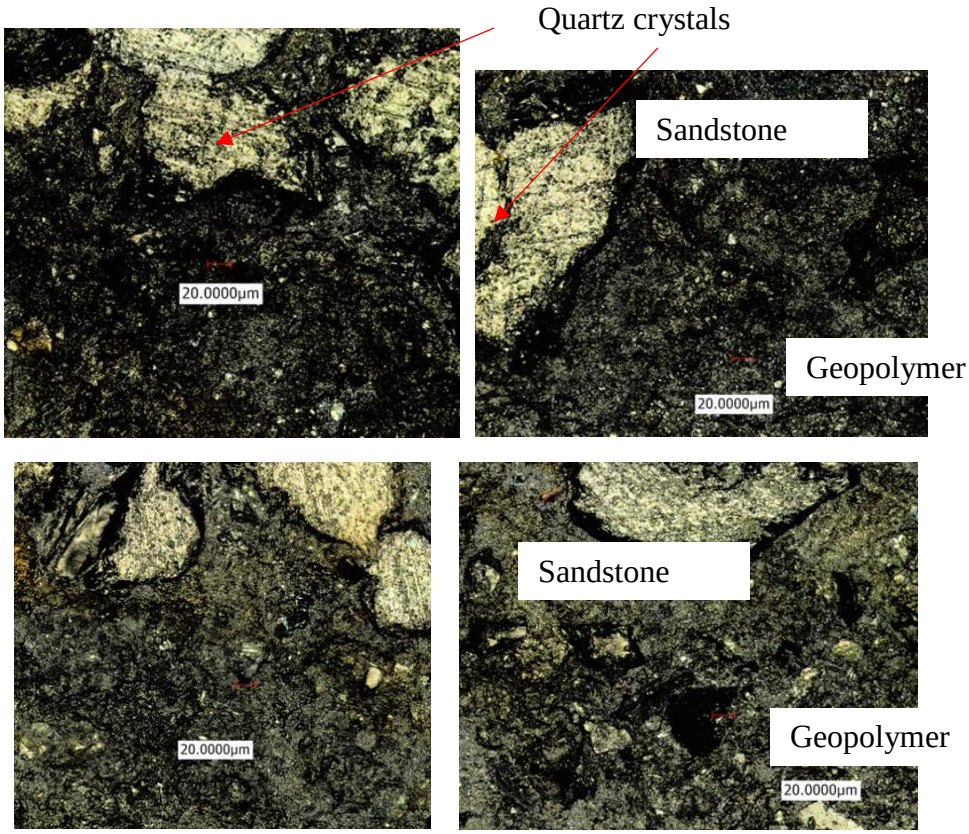

Figure B7 – Microscope images at different points of the interface between geopolymer cement (bottom layer) and sandstone (top layer)

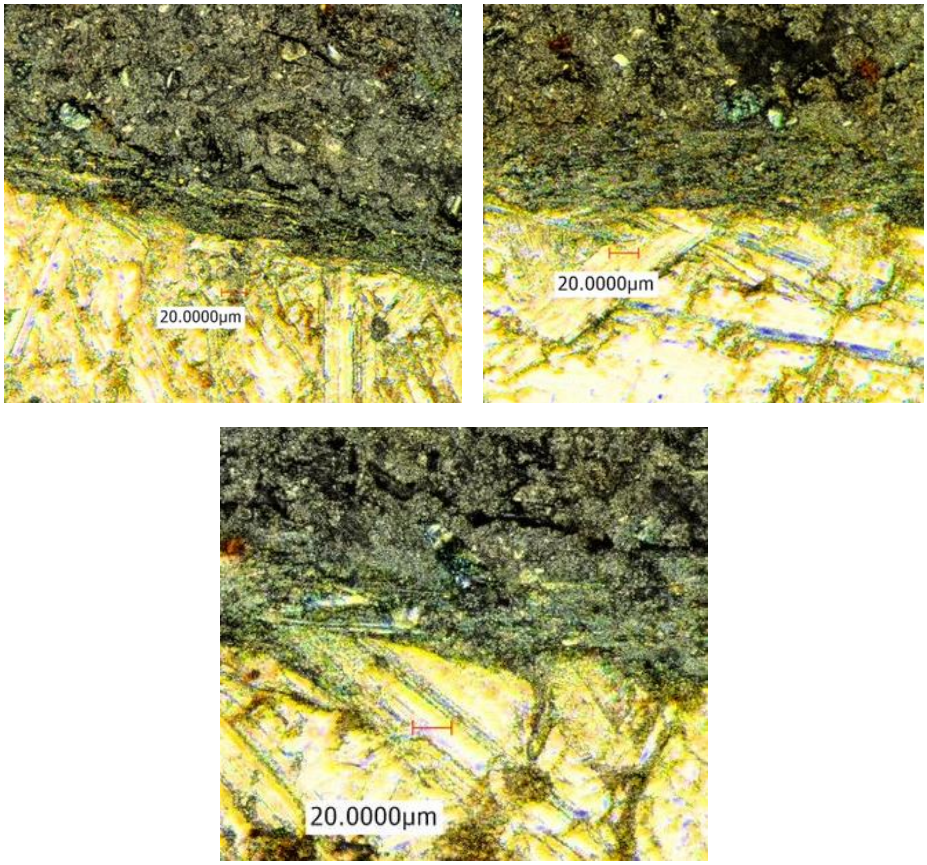

Figure B8 – Microscope images at different points of the interface between geopolymer cement (top layer) and steel (bottom layer)

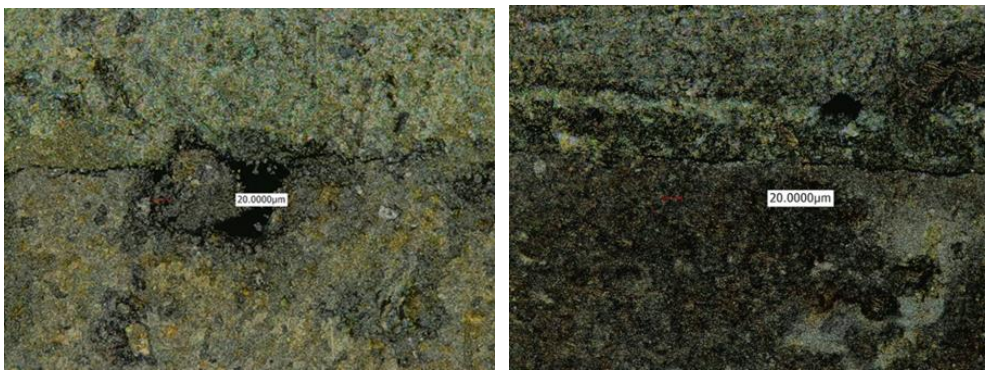

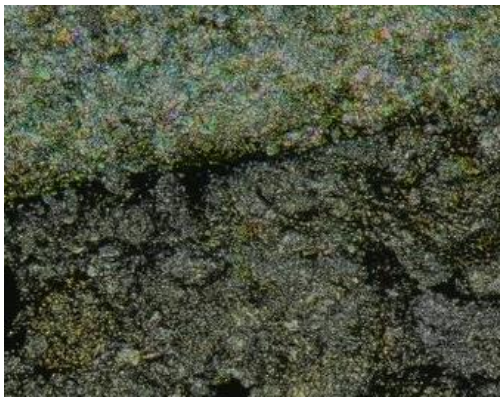

Figure B9 – Microscope images at different points of the interface between Neat class H cement (bottom layer) and shale (top layer)